

www.acsanm.org Forum Article

Molten Salt Electrolytic CO₂-Derived Carbon-Based Nanomaterials for Energy Storage and Electrocatalysis: A Review

Ao Yu, Shengwen Liu, Wei Zhang, and Yang Yang*



Cite This: https://doi.org/10.1021/acsanm.4c00010

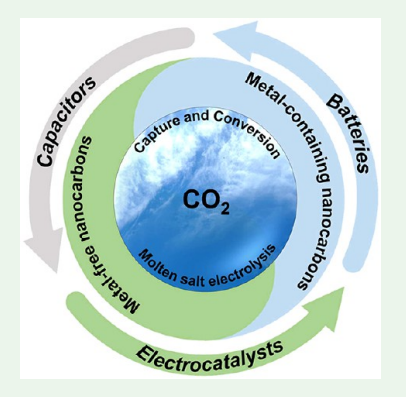


ACCESS |

III Metrics & More

Article Recommendations

ABSTRACT: The electroreduction of CO_2 in molten salt presents a promising strategy for achieving decarbonization while simultaneously producing highly valuable CO_2 -derived carbon-based nanomaterials. Although electrolytic nanocarbons have been explored for an extended period, their applications in energy storage and as electrocatalysts still require an indepth study. This paper initially introduces the advantages and basic mechanisms of CO_2 reduction in molten salt and then discusses the progress of CO_2 -derived carbon-based nanomaterials. More importantly, the paper summarizes the applications in capacitors, batteries, and electrocatalysts based on research progress and material characteristics. It is highlighted that CO_2 -derived carbon-based nanomaterials were initially used in capacitors and batteries and have recently begun to be utilized as electrocatalysts for two-electron oxygen reduction reaction, oxygen evolution reaction, and hydrogen evolution reaction. A comprehensive understanding of the synthetic mechanisms of various CO_2 -derived carbon-based nanomaterials and their applications can lay a foundation for the further development of this low-carbon-footprint process.



KEYWORDS: molten salt electrolysis, CO2, nanomaterials, capacitors, batteries, electrocatalysts

1. INTRODUCTION

Human-induced CO_2 emissions undoubtedly trigger increasing CO_2 levels in the atmosphere, which is a dominant driver of global climate change and results in serious global warming. Eliminating CO_2 emissions is a crucial action in mitigating climate change and balancing the ecosystem. Nowadays, the highly developed artificial industry and high energy consumption make it very challenging to reduce CO_2 emissions on a large scale. Therefore, there is an urgent need for the advancement of CO_2 capture and conversion technologies.

A number of studies focusing on capturing and converting CO₂ to highly valuable CO₂-derived products (for example, carbon monoxide, 3,4 urea, 5,6 methylamine, 7 formate, 8-10 carbon nanotubes (CNTs), 11 porous carbons, 12 defective carbons, 13 nickel-encapsulated octahedral carbons (Ni@OCs), 14 oxygen-rich mesoporous carbons (OMCs), 15 and MoC¹6) were reported to realize decarbonization using CO₂ as a carbon feedstock. In other words, CO₂ can also be used as a valuable carbon source for fabricating useful products. In addition, regarding commercial interests, CO₂ can be sold for about \$50/ton for the enhanced oil recovery project, which plays a pivotal role in driving the development of CO₂ capture technologies. 17,18 Electroreduction of CO₂ in molten salts has drawn great attention from researchers because of its plentiful advantages. The molten salt electrolytes commonly consist of costless inorganic salts, for example, Li₂CO₃, Na₂CO₃, K₂CO₃, CaCO₃, LiCl, NaCl, KCl, and CaCl₂. In the molten status, the

melts are made up of free ions, which ensures high ionic conductivity and charge transfer for the electrolytic process. The melt temperatures of molten salt can vary from a few tens to several hundred degrees Celsius, which means that the reaction kinetics of CO₂ electroreduction can be easily accelerated by increasing the temperature, 19,20 without concerns of high-temperature volatilization due to the high boiling points. Besides, the wide electrochemical window of molten salt can also conveniently regulate the reaction conditions and refine the resulting products. In addition, the absence of moisture in molten salt can effectively avoid the competitive hydrogen evolution reaction (HER), which in return improves the selectivity of electrochemical reactions and is beneficial to CO₂ conversion.²¹ Most importantly, no expensive and complex catalysts are necessary for the electroreduction of CO2 in molten salt, and CO2 can be directly and easily reduced on a conductivity substrate. Although CO₂ can also be electroreduced in aqueous liquids (ALs) and room temperature ionic liquids (RTILs), those

Special Issue: Low-Dimensional Nanomaterials and Their Assembled Structures and Interfaces for Energy Applications

Received: January 1, 2024 Revised: February 1, 2024 Accepted: February 5, 2024



Table 1. Summary of the CO₂-C-Based Materials for Capacitors

product	electrolyte	ama aifi a aama aitus	stability	al a atma livita	*****	ref
•	electrolyte	specific capacity	′	electrolyte	year	rei
3D SPC (three or two- electrode cell)	Li ₂ CO ₃ -Na ₂ CO ₃ -K ₂ CO ₃ (30.5:11:8.5 wt %)	373.7 F g ⁻¹ (0.5A g ⁻¹), 336.0 F g ⁻¹ (0.2A g ⁻¹)	95.9% (10 A g ⁻¹ , 10000 cycles), 91.1% (5 A g ⁻¹ , 15000 cycles)	6 М КОН	2021	12
amorphous carbon (three-electrode cell)	Li ₂ CO ₃ -Na ₂ CO ₃ -K ₂ CO ₃ (43.5:31.5:25 mol %)	400 F g ⁻¹ (0.2A g ⁻¹), 376 F g ⁻¹ (0.5A g ⁻¹)		1 M H ₂ SO ₄	2013	48
amorphous carbon (three-electrode cell)	Li ₂ CO ₃ -Na ₂ CO ₃ -K ₂ CO ₃ (43.5:31.5:25 mol %)	$550 \text{ F g}^{-1} (0.2 \text{A g}^{-1})$	73% (4A g ⁻¹ , 10000 cycles), 59% (10 A g ⁻¹ , 10000 cycles)	1 M H ₂ SO ₄	2019	51
amorphous carbon (three-electrode cell)	Li ₂ CO ₃ -Na ₂ CO ₃ -K ₂ CO ₃ (43.5:25:31.5 mol %)	$410 \text{ F g}^{-1} (5 \text{ mV s}^{-1})$		0.5 M H ₂ SO ₄	2020	96
amorphous carbon (three-electrode cell)	Li ₂ CO ₃ -Na ₂ CO ₃ -K ₂ CO ₃ (43.5:25:31.5 mol %)	$375 \text{ F g}^{-1} (10 \text{ mV s}^{-1})$		0.5 M H ₂ SO ₄	2018	97
amorphous carbon (three-electrode cell)	Li ₂ CO ₃ -Na ₂ CO ₃ -K ₂ CO ₃ (43.5:25:31.5 mol %)	$450 \text{ F g}^{-1} (0.0833 \text{ m V} \text{ s}^{-1})$	/	0.5 M H ₂ SO ₄	2018	98
S-doped carbon (two- electrode cell)	Li ₂ CO ₃ -Na ₂ CO ₃ -K ₂ CO ₃ - Li ₂ SO ₄ (40.02:28.98:23:8 mol %)	257.3 F g ⁻¹ (0.2A g ⁻¹)	93.1% (10 A g ⁻¹ , 10000 cycles)	1 M H ₂ SO ₄	2017	53
amorphous carbon (two-electrode cell)	Li ₂ CO ₃ -Na ₂ CO ₃ -K ₂ CO ₃ (43.5:31.5:25 mol %)	240 F g ⁻¹		6 М КОН	2016	99
	LiCl-KCl-Li ₂ CO ₃ (58.5:41.5:2 mol %)	102 F g ⁻¹				
	LiCl-KCl-CaCO ₃ (58.5:41.5:2 mol %)	145 F g^{-1} (0.2 A g^{-1})				
hollow carbon spheres (two-electrode cell)	2 mol % CaCO ₃ -containing LiCl– KCl (58.5:41.5 mol %)	$171 \text{ F g}^{-1} (0.2 \text{ A g}^{-1})$		6 М КОН	2017	52
O-rich carbon (ZIC)	Li ₂ CO ₃ -Na ₂ CO ₃ -K ₂ CO ₃ (43.5:31.5:25 mol %)	$257 \text{ mAh g}^{-1} (0.05 \text{ A g}^{-1})$	62% (1 A g ⁻¹ , 2000 cycles)	2 M Zn(CF ₃ SO ₃) ₂	2022	63
O-rich mesoporous carbon (ZIC)	Li ₂ CO ₃ -Na ₂ CO ₃ -K ₂ CO ₃ (30.5:11:8.5 wt %)	(0.25 A) mAh g^{-1} (0.25 A)	90% (2 A g ⁻¹ , 15000 cycles)	2 M ZnSO ₄	2023	15

strategies suffer from lots of challenges. Regarding the electroreduction of CO₂ in ALs, a seriously competitive HER occurs due to the close reduction potential of CO2 to the hydrogen evolution,² which also leads to a narrow electrochemical window due to the reaction occurring in water. In addition, CO₂ shows low solubility and slow kinetics in ALs, and the reaction should be driven by complex and expensive catalysis as well. $^{22-32}$ Those limitations potentially result in a low faraday efficiency. Although some progress has been made in converting CO2 into valuable chemicals in low-cost ALs, 30-32 [for example, a noble-metal PdBi alloy anchoring on a carbon substrate (BiPdC) is constructed for the carbon dioxide reduction reaction (CO₂RR) and formic acid oxidation (FAO) by effectively overcoming the sluggish kinetics of CO₂RR and FAO³¹], there are still challenges in converting CO₂ to useful solid carbon-based nanomaterials. On the other hand, although the electroreduction of CO₂ in RTILs can overcome the competitive HER and enlarge the electrochemical window, it is important to note that there are many challenges for the RTILs including their cost, toxicity, and environmental impact.³³ Additionally, the choice of RTILs and their compatibility with specific electrocatalysts are also still unclear. Herein, only the electroreduction of CO2 in molten salt is discussed in this paper.

In earlier studies involving the electroreduction of CO_2 in molten salt, the products are mainly metal-free CO_2 -derived nanocarbons (CO_2 -C) with irregulated morphologies, which are mainly used for energy storage including supercapacitors and Li/Na-ion batteries (LIBs/SIBs) due to the intrinsic characteristics of nanocarbons (for example, stable chemical properties, good conductivity, abundant surficial oxygen functional groups, etc.), as summarized in Tables 1–3. However, the specific capacities of metal-free CO_2 -C in LIBs are relatively lower, prompting further explorations of incorporating active metals to enhance the capacitive performance. For instance, metals such as Ge, Sn, Zn, and Fe have

been introduced to CO_2 -C to synthesize metal@CNTs or metal@carbon spheres through the coreduction of CO_2 and metal oxides (GeO₂, SnO₂, ZnO, and FeO) or utilization of a liquid zinc anode, thereby enhancing the LIBs' performance. ^{14,34,35}

Regarding the applications of electrocatalysts, there have been few reports on employing metal-free CO2-C as electrocatalysts. To date, only approximately two studies have concentrated on its application in the two-electron (2e) oxygen reduction reaction (ORR). 11,13 This is attributed to the fact that the inherent O doping and defects in metal-free CO₂-C can serve as active sites for the 2e ORR. In the last 5 years, the as-prepared CO₂-C has started to become more controllable with regulated morphologies on a large scale. For example, highly ordered porous C, 12 industrial-grade CNTs, 36 and core-spherical metal/carbon composites 14 etc., were reported. Notably, significant advancements in the development of CO₂-C since 2019 have been made through the introduction of metals, which has considerably expanded the variety of CO₂-C (namely, metal-containing CO₂-C and composites have started to emerge) and led to substantial innovations in applications (Figure 1). As summarized in Table 1-3, active metals including Fe, Co, Ni, and Mo have been effectively integrated into CO2-C, facilitating the synthesis of

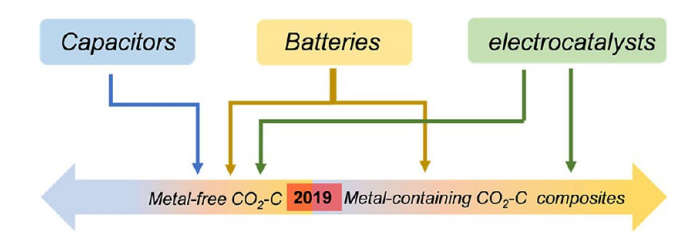


Figure 1. Overview of the CO₂-C-based materials and their applications.

 $\rm CO_2$ -C-based nanomaterials via the coreduction of $\rm CO_2$ and high-valence-state metallic elements and the combination of electroreduction of $\rm CO_2$ and thermochemical reaction between the metal source and electrolytic C. The electrolytic coreduction of $\rm CO_2$ and $\rm Fe_2O_3$ results in the formation of $\rm Fe/Fe_3C$ -modified C, which notably enhances the oxygen evolution reaction (OER) performance. In this process, the addition of Fe is crucial for this improvement. Similarly, direct electroreduction of $\rm CO_2$ on a Mo plate cathode leads to the creation of a $\rm MoC$ -Mo $_2$ C nanocomposite through thermochemical reactions between Mo atoms and electrolytic C atoms, thereby significantly improving the HER performance. Although the application of $\rm CO_2$ -C-based nanomaterials has been explored with great achievements, they are still limited to the 2e ORR, OER, and HER.

The development of applications for CO_2 -C-based nanomaterials through molten salt electrolysis has been rapidly advancing, particularly in the last 5 years. Numerous reviews on the reaction mechanisms and types of materials prepared from electrolytic carbon have been discussed. However, the burgeoning research on applications for these CO_2 -C-based nanomaterials is only in its nascent stages. Creating a detailed and systematic classification of the reported applications of CO_2 -C-based nanomaterials is crucial for a comprehensive understanding of the evolution of this exciting field. This paper initially addresses the inherent advantages of molten salt as a medium for CO_2 electroreduction compared to alternative methods. Subsequently, it delves into the research progress of CO_2 -C-based nanomaterials, shedding light on their applications and potential material design strategies.

2. REACTION MECHANISMS OF THE ELECTROREDUCTION OF CO₂ IN MOLTEN SALT

Molten salt CO_2 electrolysis represents a dual-purpose approach involving CO_2 capture and its subsequent electrochemical conversion into valuable products including solid carbon, oxygen, and CO_2^{0} . The electroreduction of CO_2 within a molten salt environment occurs through a two-step process comprising capture and conversion. CO_2 capture involves consecutive carbonation reactions, while conversion entails the electroreduction of carbonate ions, resulting in an overall net reduction of CO_2 . In CO_3^{2-} -containing molten salt, CO_3^{2-} spontaneously undergoes an equilibrium decomposition reaction $(\mathrm{CO}_3^{2-} \leftrightarrows \mathrm{CO}_2 + \mathrm{O}^{2-})^{41-44}$ Such intrinsic O^2- and CO_3^{2-} sever as receptors to capture CO_2 as follows: 41,42,45,46

$$CO_2 + O^{2-} = CO_3^{2-}$$
 (1)

$$CO_3^{2-} + CO_2 = C_2O_5^{2-}$$
 (2)

Here, although both O^{2-} and CO_3^{2-} contribute to the capture of CO_2 , O^{2-} dominates the capture process due to the stronger coordination between O^{2-} and CO_2 . CO_3^{2-} is electroreduced on the cathode through the following two reactions:⁴⁰

two-electron pathway:
$$CO_3^{2-} + 2e = CO + 2O^{2-}$$

(T > 850 °C) (3)

four-electron pathway:

$$CO_3^{2-} + 4e = C + 3O^{2-} (T < 850 \, ^{\circ}C)$$
 (4)

In addition, molten carbonates can provide about 20 mol of reducible tetravalent carbon per liter, the concentration of which is about 1.18×10^6 -fold than the atmospheric reducible tetravalent carbon. ⁴⁷ Such a high concentration of reducible tetravalent carbon ensures an abundant carbon source for reduction, and the simultaneously generated O^{2-} rapidly captures the ambient CO_2 to replenish the consumed CO_3^{2-} in the melt (see eq 1). Regarding the molten halides, the lack of a CO_2 trapping agent makes it impossible to electroreduce CO_2 effectively unless carbonates or alkaline oxides are purposely added to the melts. Generally, some carbonates, including $CaCO_3$, Li_2CO_3 , Na_2CO_3 , and K_2CO_3 , and alkaline oxides, including CaO and Li_2O , are added to molten halides to capture CO_2 for subsequent electrochemical reductions.

It can be found that cathodic reductions inevitably generate O^{2-} , some of which is used as a CO_2 trapping agent to capture CO_2 . The excess O^{2-} is oxidized to oxygen at the anode as follows.

$$2O^{2-} - 4e = O_2 (5)$$

Therefore, the net reactions of CO₂ reduction in molten salt can be written as follows:

$$CO_2 = CO + \frac{1}{2}O_2 (T > 850 \,^{\circ}C)$$
 (6)

$$CO_2 = C + O_2 (T < 850 \,^{\circ}C)$$
 (7)

The state of the products in the net reactions is significantly influenced by the reaction temperature. Lower reaction temperatures are advantageous to produce solid carbon products, whereas elevated temperatures exceeding 850 $^{\circ}\text{C}$ favor the generation of gaseous products. To obtain CO₂-C-based nanomaterials in molten salts, the electrolysis temperatures should be lower than 850 $^{\circ}\text{C}$.

In addition to the temperature, the inlet gas rate and CO₂ concentration can affect the competitive reactions: two- or four- electron reactions, as given in eqs 3 and 4. The intensifying gas flow rates can enhance the transformation of CO₂ to CO to a certain extent by improving the interaction between the gas and molten salts as well as enhanced ion dispersion. This process inhibits the deposition of solid nanocarbons on the cathode due to the reduced residence time of CO₂ in molten salt.⁴ On the other band, the effects of various CO₂ concentrations ranging from 0.04% (akin to atmospheric levels) to 14% (representative of CO₂ concentrations in flue gases) and up to 100% on the synthetic products were studied. 47-49 The preliminary concentration of CO₂ prior to the electrolysis process is not considered necessary. Research has shown that around 50% of CO₂ at a 14% concentration can be effectively absorbed from the gas phase and converted into carbon, achieving a notable current efficiency of 90%.⁴⁹ Furthermore, even at the minimal CO₂ concentration of 0.04%, bypassing the concentration step does not adversely affect the electrolytic process, allowing maintenance of the current efficiencies near 100%. 18 Regarding the effects of other gaseous impurities, only SO2 and vapor were studied in molten electrolysis. A mixture of SO₂ and CO₂ fed into a Li₂CO₃-Na₂CO₃-K₂CO₃-Li₂SO₄ electrolyte resulted in the preparation of S-doped carbon through the coreduction of SO_4^{2-} and CO_3^{2-} in the electrolyte.⁵⁰ Here, the gaseous SO_2 was used to replenish the consumed Li_2SO_4 (O^{2-} + SO_2 + $0.5O_2$ = SO_4^{2-} ; CO_3^{2-} + SO_2 + $0.5O_2$ = SO_4^{2-} + CO₂). The vapor was only applied in MOH (M = alkaline metal) containing carbonates for synthesizing syngas. In such an electrolysis, H2 is the main product in most cases when CO2

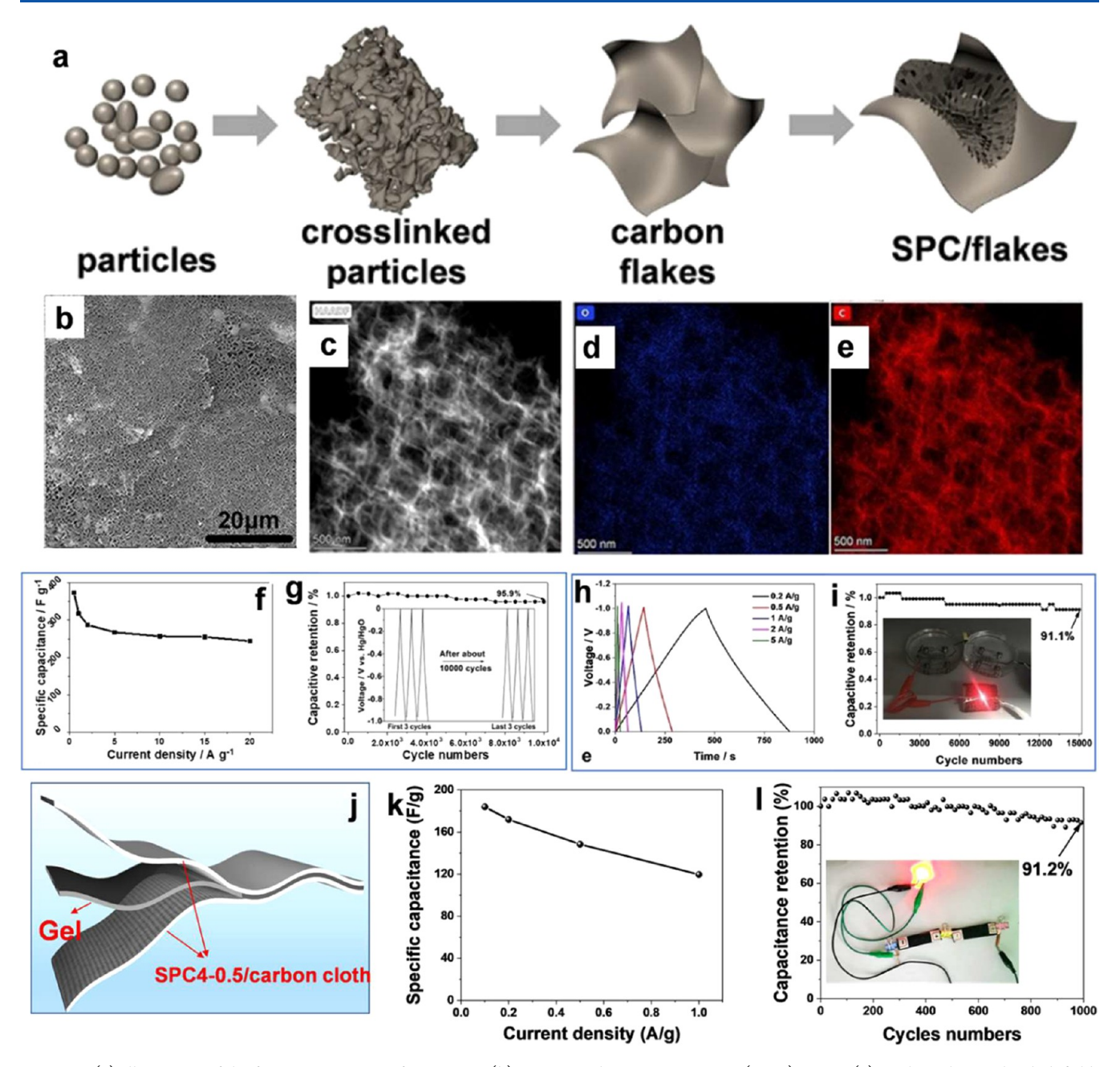


Figure 2. (a) Illustration of the formation process of a 3D SPC. (b) Scanning electron microscopy (SEM) image. (c) High-angle annular dark field-scanning transmission electron microscopy (HAADF-STEM) image. (d) Oxygen and (e) carbon distribution of SPC4-0.5. (f) Rate performance and (g) cycling stability of SPC4-0.5 in a three-electrode cell. (h) Gravimetric specific capacitance curves and (i) cycling stability of SPC4-0.5 in a quasi-solid-state symmetric supercapacitor. (j) Illustration of an all-solid-state flexible supercapacitor (ASS-FS). (k) Rate performance and (l) cycling stability of an ASS-FS device. Reprinted with permission from ref 12. Copyright 2021 Wiley-VCH GmbH.

and vapor are fed to molten carbonates with MOH additives. ⁴⁰ The reaction mechanisms of syngas are given below. In conclusion, with respect to the synthesis of solid carbon nanomaterials, foreign gases may exert limited effects on the resulting products. As summarized in Tables 1–3, beyond temperature considerations, the regulatory focus on molten salt electrolysis centers on the composition of electrolytes and electrodes that directly influence the liquid/solid reaction interface.

$$M_2CO_3 + 2MOH = 2M_2O + CO + H_2 + O_2$$
 (8)

$$3M_2O + CO_2 + 2H_2O = M_2CO_3 + 4MOH$$
 (9)

$$M_2CO_3 + 4MOH = 3M_2O + CH_4 + 2O_2$$
 (10)

$$CO_2 + 2H_2O = CH_4 + 2O_2$$
 (11)

Here, M represents the alkaline metal.

3. APPLICATIONS OF ENERGY STORAGE AND ELECTROCATALYSIS

The applications of CO_2 -C-based nanomaterials span various domains, including supercapacitors, Zn-ion capacitors (ZICs), LIBs, SIBs, and Al-ion batteries (AlIBs), as well as in the 2e ORR, OER, and HER (Tables 1–3). Initially, most electrolytically derived CO_2 -based nanomaterials were metal-free

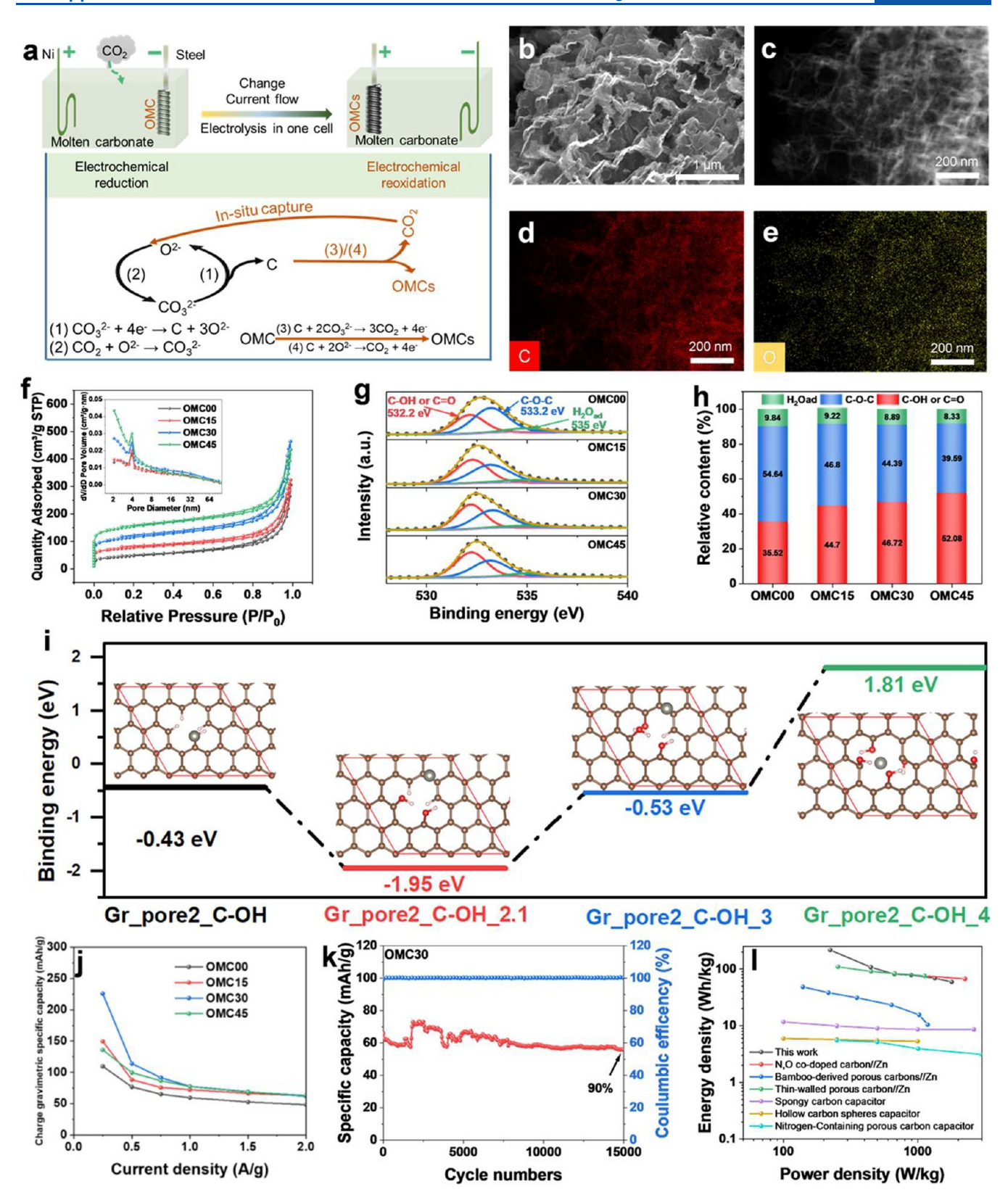


Figure 3. (a) Synthetic process of OMCs. (b) SEM and (c) HAADF-STEM images and corresponding elemental mappings of (d) carbon and (e) oxygen. (f) N_2 adsorption and desorption isotherms. Inset: Pore-width distributions of OMCs (Barrett-Joyner-Halenda method). (g) O 1s X-ray photoelectron spectroscopy (XPS) spectra and (h) relative content of different oxygen functional groups of OMCs. (i) Binding energy of a geometrical configuration of a Zn atom adsorbed on different configurations. (j) Rate performance of OMCs. (k) Cycling stability of OMC30 at 2 A g^{-1} . (l) Ragone plot. Reprinted with permission from ref 15. Copyright 2023 Wiley-VCH GmbH.

nanocarbons, typically featuring porous or irregular structures, and were predominantly utilized in capacitors and LIBs.

However, over the past 5 years, numerous studies have begun incorporating active metals into the molten system to create

metal-containing CO₂-C nanocomposites (carbon-metal hybrid nanomaterials), aiming to investigate their potential in optimized LIBs, AlIBs, and electrocatalysts.

3.1. Capacitors. Molten salt electrolytic CO₂-C have found extensive applications in supercapacitors over an extended period due to their diverse structures, abundant morphologies, highly active surfaces, excellent electrical conductivity, and strong chemical stability. The relatively early exploration of CO₂-C for capacitors dates back to 10 years ago, as shown in Table 1. For instance, amorphous carbon powder synthesized from a melt of Li₂CO₃-Na₂CO₃-K₂CO₃ (at 500 °C) by employing a Ni cathode and a SnO₂ anode (cell voltage: 4.0 V) exhibits a remarkable Brunauer-Emmett-Teller (BET) surface area exceeding $400 \text{ m}^2 \text{ g}^{-1}$ and demonstrates a specific capacitance of $400 \text{ F g}^{-1} (0.2 \text{ A g}^{-1})$ in a $1 \text{ M H}_2 \text{SO}_4$ aqueous solution.⁴⁸ Through optimization of experimental parameters, including raising cell voltages to 4.5 V and decreasing operating temperatures to 450 °C, the specific capacitance of the CO₂-C can be elevated to as high as 550 F g⁻¹ (0.2 A g⁻¹).⁵¹ In addition, the performances of symmetrical full supercapacitors have also been studied. A hollow carbon sphere synthesized by constant-voltage electrolysis in 2 mol % CaCO₃-containing LiCl-KCl at 450 °C for 1 h derived a specific capacitance of 171 F g⁻¹ at 0.2 A g⁻¹ in 6 M KOH when assembled as a symmetrical full supercapacitor. 52 Interestingly, Wang et al. applied a Li₂CO₃-Na₂CO₃-K₂CO₃-Li₂SO₄ molten salt to cocapture CO₂ and SO₂ for electrolysis, resulting in an S-doped porous carbon. SO_4^{2-} in molten salt is reduced to S and S^{2-} , which could facilitate S doping in carbon.⁵³ At the same time, the bubbled gaseous SO₂ is captured by CO_3^{2-} and O^{2-} to replenish SO_4^{2-} [CO_3^{2-} + $SO_2(g)$ + $0.5O_2$ = SO_4^{2-} + $CO_2(g)$; O^{2-} + $SO_2(g)$ + $O_2(g)$ = SO_4^{2-}]. Such S-doped porous carbon with intriguing physicochemical properties and enhanced functionality demonstrated a better capacitance of 257.3 F g⁻¹ (0.2 A g^{-1}) than that of S-free carbon (approximately 215 F g^{-1} at 0.2 A g^{-1}) when used as a symmetrical full supercapacitor.

Although CO₂-C has been confirmed with its capacitive performance, the research process in this area is still sluggish. In addition, most reported CO₂-C are amorphous carbon with an irregulated structure, for example, carbon sheets or carbon particles, which probably impedes the deep exploration of those nanocarbons as an effective material for capacitors. A systematic exploration of CO₂-C for capacitors seems to have been rarely reported until Li et al. systematically explored 3D spongy mesoporous/microporous carbon (SPC) as active materials for capacitors. 12 Such nanocarbons were obtained by electrolysis in molten Li₂CO₃-Na₂CO₃-K₂CO₃ at 580 °C using Ni and steel as the anode and cathode, respectively. During electrolysis, a thin carbon flake is first deposited onto the steel cathode as a substrate for the subsequent generation of porous carbon (Figure 2a) and then formation of a 3D SPC on a large scale (Figure 2b,c). Furthermore, the electroreduction of CO2 in molten ternary carbonate can achieve a high productivity of 96.9%, indicating the highly efficient utilization of CO₂. Such a 3D SPC enables a large electrolyte ion-accessible surface. The O element is found to be uniformly dispersed on the carbon farmwork (Figure 2d,e), which can enhance the wettability of the as-prepared 3D carbon and facilitate the capacitive performance. In a three-electrode cell, the specific capacitance of SPC4-0.5 (electrolysis at 4 A for 0.5 h) demonstrates a high specific capacitance of 373.7 F g⁻¹ (0.5A g⁻¹) and an excellent cycling stability of 95.9% (10 A

g⁻¹, 10000 cycles) (Figure 2f,g). When SPC4-0.5 is assembled into a quasi-solid-state symmetric supercapacitor, it demonstrates a high specific capacitance of 336.0 F g⁻¹ (0.2 A g⁻¹) (Figure 2h,i). In addition, even if SPC4-0.5 was assembled into an all-solid-state capacitor, it can also deliver a high capacitance of 183.9 F g⁻¹ (0.1 A g⁻¹) and a capacitance retention of 91.1% after 1000 cycles (Figure 2j–l). Although the capacitive performance of such a 3D SPC is superior to that of other reported CO_2 -C, its application still needs further exploration.

In general, carbon-based supercapacitors are criticized for their low energy density, typically ranging from 5 to 8 Wh kg^{-1.54} This limitation significantly hinders their potential for use in next-generation energy storage. Hybrid ZICs have received considerable research focus due to their affordability, 55 impressive theoretical capacity of 820 mAh g⁻¹, 56 and exceptional chemical stability in aqueous electrolytes. 57,58 These characteristics make it possible to achieve both high power and high energy densities by pairing Zn anodes with capacitive cathodes in ZICs. The overall ZICs performance of carbon materials relies on the proper mesopore structure and surface functional groups, which provide short diffusion paths for enhancing ion and electrolyte transport and pseudocapacitive redox reactions. Surface functionalization of carbons with oxygen-containing functional groups, such as C-OH and C= O, is advocated as an ancillary strategy to modulate and amplify the pseudocapacitive behavior of ZICs. 59,60 This enhancement occurs through the following reactions: C + X-= X-C (X⁻: anions) and C-OH + Zn^{2+} + 2e = C-O-Zn or C-OH + Zn^{2+} + e = C-O-Zn + H⁺.61,62 Although the oxygen-containing carbons have many advantages for ZICs, only a few works about the CO₂-C were reported. 15,63 Li and Yang et al. reported a CO₂-derived OMC for ZICs. 15 OMC was innovatively obtained through bidirectional electrolytic reduction of CO₂ in a molten Li₂CO₃-Na₂CO₃-K₂CO₃. As illustrated in Figure 3a, CO₂ is initially reduced to solid carbon on the steel cathode. Then, the deposited carbon is used as an anode by reversing the current flow. During anodic polarization, carbon undergoes etching processes $(C + 2CO_3^2)^2$ $3CO_2 + 4e$ and $C + 2O^{2-} = CO_2 + 4e$), leading to the formation of abundant microstructures. These include an increased specific surface area (SSA) and modification of the surface oxygen functional groups. The prepared OMC30 exhibits a porous structure with O elements uniformly distributed on the carbon substrate, as shown in Figure 3be. The SSA of the OMCs demonstrated a positive correlation with the extended duration of reoxidation, facilitating exposure of a greater number of zincophilic sites to Zn ions. Furthermore, it is the reoxidation process that regulates the variations in the different oxygen functional groups (Figure 3f-h). As the reoxidation period is extended, a notable decrease in the C-O-C content is observed, while the levels of C-OH and C=O correspondingly increase, indicating a shift in the chemical composition (Figure 3h). The systematic density functional theory (DFT) calculations reveal that the mode of two identical -OH functional groups in the para position on Gr_pore2 exhibits the most pronounced zincophilicity among various configurations. This finding underscores the importance of the appropriate content and type of oxygen functional groups for optimal ZIC performance, as illustrated in Figure 3i. The obtained OMC30 (reoxidation at 0.5 A for 30 min) exhibits the largest specific capacitance of 242.0 mAh g⁻¹ among the four samples and can achieve a capacitance retention of 90% at 2 A g⁻¹ after 15000 cycles

Table 2. Summary of CO₂-C-Based Nanomaterials for Batteries

product	electrolyte	electrolysis conditions ^a	specific capacity	year	electrolyte	ref
spherical carbon particles	LiCl-Li ₂ CO ₃ (1, 5, 10 mol %)	700 °C, 2.2 V, anode = Pt wire, cathode = W wire	318 mAh g ⁻¹ (50 mA g ⁻¹), 215.5 mAh g ⁻¹ (500 mA g ⁻¹)	2015	1 M LiPF,	29
CNTs	${ m Li_2CO_3-Li_2O}$	750 $^{\circ}\text{C}_{\nu}$ 1 mA for 0.5 h and 1 A for 1 h, anode = Ni wire, cathode = steel wire	LIBs: 370 mAh g^{-1} (100 mA g^{-1}) SIBs: 130 mAh g^{-1} (100 mA g^{-1})	2016	1 M LiPF $_{6}$ and NaPF $_{6}$	69
amorphous carbon	Li ₂ CO ₃ -Na ₂ CO ₃ -K ₂ CO ₃ (43.5: 31.5:25 mol %)	450 °C, 4.5 V, anode = SnO_2 rod, cathode = Ni plate	798 mAh g ⁻¹ (50 mA g ⁻¹)	2017	$1~\mathrm{M}~\mathrm{LiPF_6}$	100
hollow carbon spheres	LiCI-KCI-2 mol % CaCO ₃	450 °C, 2.8 V, RE = Ag/AgCl, WE = Ni wire, CE = graphite rod	550 mAh g ⁻¹ (50 mA g ⁻¹)	2018	1 M LiPF ₆	89
Ge@CNT	NaCl–CaCl ₂ –CaO–CeO ₂ (NaCl:CaCl ₂ = 48:52 wt %, 2 wt % CaO, and 0.3 wt % of GeO ₂)	750 °C, 2.2 V, anode = graphite rod, cathode = Ni plate	$801 \text{ mAh g}^{-1} (200 \text{ mA g}^{-1})$	2020	1 M LiPF ₆	34
Sn@CNT	337 g of CaCl ₂ –163 g of NaCl–20 g of CaO containing 2 g of SnO ₂ /ZnO/FeO	$Sn @ CNT$: 2.8 V for 2 h in 800 °C molten $CaCO_3-Na_2CO_3-K_2CO_3-SnO_2$ using a Ni sheet cathode and an inert $Ni_{11}Fe_{10}Cu$ anode	Sn@CNT: 510 mAh g ⁻¹ at 1000 mA g ⁻¹ after 400 cycles	2023	1 M ${ m LiPF}_6$	35
Zn@CNT		Zn@CNT: 2.4 V for 2 h in 800 °C molten CaCl ₂ —NaCl—CaO—ZnO using a carbon paper cathode and a graphite anode				
Fe@CNT		Fe@CNT: 2.4 V for 2 h in 800 °C molten CaCl,—NaCl—CaO—FeO using a carbon paper cathode and a graphite anode				
Ni@OC	$Li_2CO_3-Na_2CO_3-K_2CO_3$ (61:22:17 wt %)	2° 088	433.6 mAh g ⁻¹ (25 mA g ⁻¹)	2023	1 M LiPF_6	14
		step I: 4 A, 0.5 h	capacity retention: 83.3% (4800 cycles)			
		step II: 0.5 A, 2 h				
Sn@C/C flakes	Li ₂ CO ₃ -Na ₂ CO ₃ -K ₂ CO ₃ (32:33:35 mol %)	500 °C, 2.2 V for 3 h, anode = Mo, cathode = liquid Sn	$515 \text{ mAh g}^{-1} \text{ after } 800 \text{ cycles}$ at 500 mA g^{-1}	2023		72
$Z_{\rm n}$ $@C/PC$	$Li_2CO_3-Na_2CO_3-K_2CO_3$ (1:1:1 wt %)	450 °C, 1 A for 1 h, anode = liquid Zn, cathode = steel	1271 mA h g ⁻¹ at 50 mA g ⁻¹	2023	1 M LiPF ₆	73
Zn@graphitic carbon	Li ₂ CO ₃ -Na ₂ CO ₃ -K ₂ CO ₃ (32:33:35 wt %)	-0.9~V vs Ag/Ag ₂ SO ₄ , 450 °C for 3 h, CE = Pt@Ti plate, WE = liquid Zn	$\approx 90 \text{ mAh g}^{-1} \text{ after } 450 \text{ cycles}$	2020	AlCl ₃ and 1-ethyl-3-methylimidazalium chloride mixed in a molar ratio of 1.3:1	74
antf	and the section of th					

 $^a\mathrm{RE}\mathrm{:}$ reference electrode. WE: working electrode. CE: counter electrode.

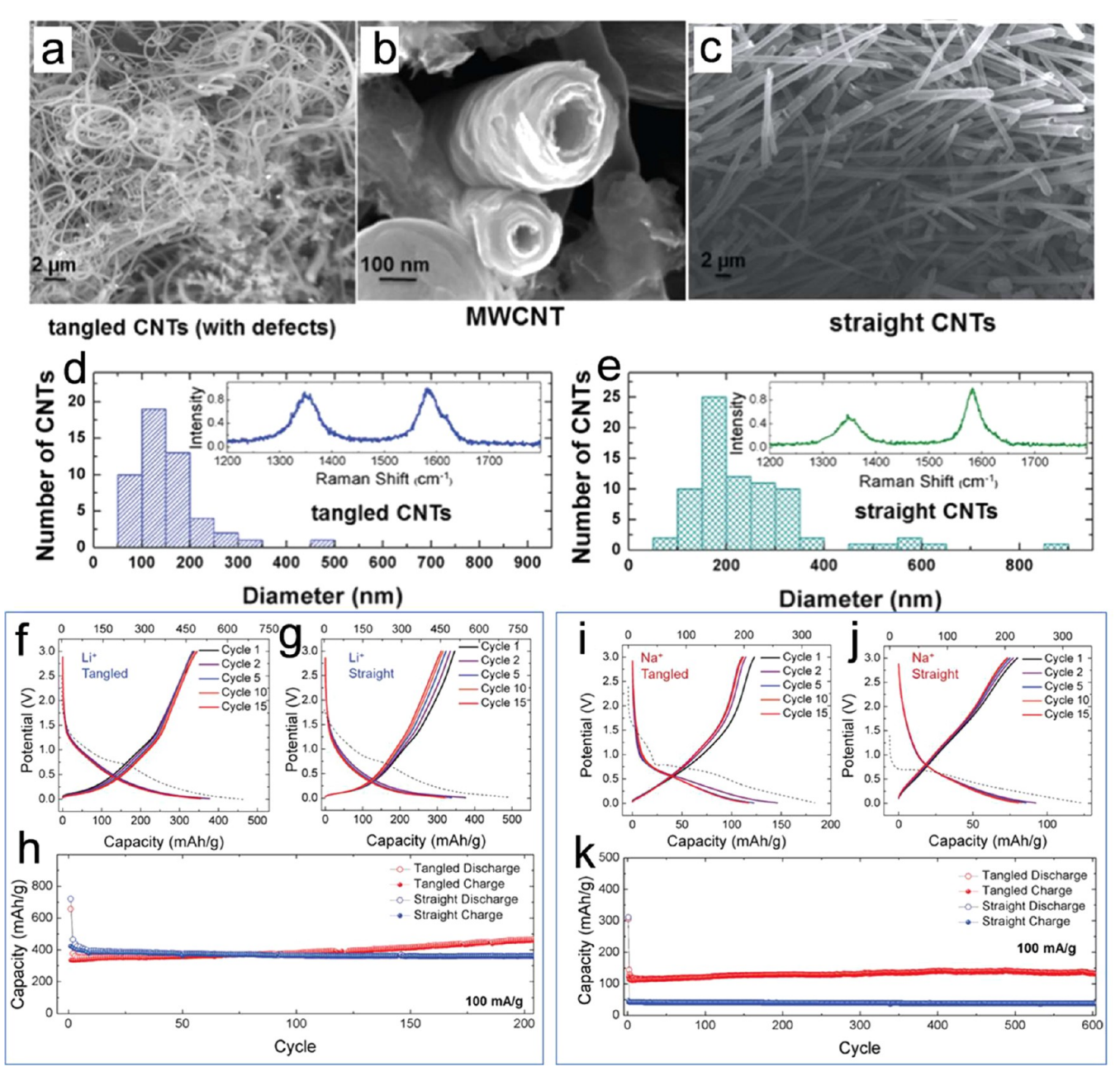


Figure 4. (a and b) SEM images of tangled CNTs. (c) SEM image of straight CNTs. Diameter distribution of (d) tangled and (e) straight CNTs and (insets) Raman spectra of the two CNTs. (f-h) LIBs' and (i-k) SIBs' performances of tangled and straight CNTs. Reproduced from ref 69. Copyright 2016 American Chemical Society.

(Figure 3j,k). The trend in capacitance follows the order OMC30 > OMC45 > OMC15 > OMC00, indicating that an increased content of C–OH (or C=O) can enhance the Zn storage performance to a certain extent, while an excess of C–OH (or C=O) tends to weaken the capacitance. In addition, OMC30 demonstrates a high energy density of 206.1 Wh kg $^{-1}$ at a power density of 212.5 W kg $^{-1}$ (Figure 3l), which is better than those of some reported carbon materials.

3.2. Batteries. To date, CO₂-derivated carbon-based nanomaterials have been reportedly applied for LIBs, SIBs, and AlIBs, as shown in Table 2. The research progress in electrolytic nanocarbons has evolved from metal-free CO₂-C to metal-containing CO₂-C over the years. Initially, research endeavors were concentrated on the application of CO₂-C in LIBs, likely motivated by the dominant employment of

graphite as the material in these energy storage systems. At the same time, this research direction was partly driven by the goal of finding practical uses for these carbon nanomaterials. However, most CO₂-C nanomaterials are metal-free carbons with limited specific capacity. This limitation can likely be attributed to the inherent constraints of carbon, including its theoretical capacity of 372 mAh g⁻¹, disordered microstructures, and intrinsic sluggishness for ZIBs. Nevertheless, substantial efforts have been dedicated to exploring the potential of CO₂-C for ZIBs by manipulating its microstructures. For instance, when a W cathode and a Pt anode are used for electrolysis in molten LiCl-Li₂CO₃, the morphological characteristics of the resulting carbon nanomaterials exhibit limited variation under different conditions. These materials predominantly exhibit "quasispherical" microstruc-

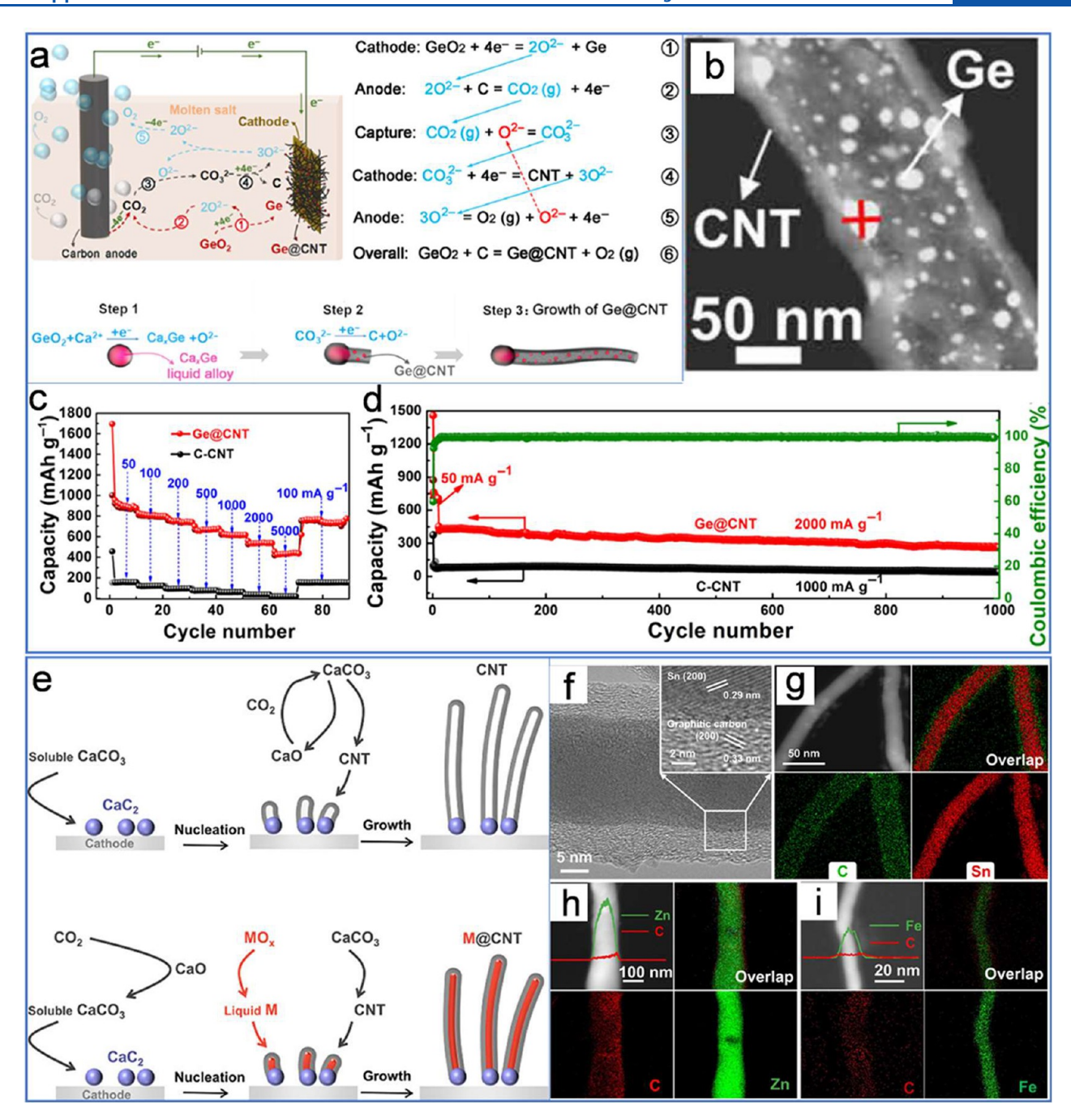


Figure 5. (a) Cathode—anode synergistic mechanisms and evolution of morphology. (b) SEM images, (c) rate performance, and (d) cycling stability of Ge@CNTs. Reprinted with permission from ref 34. Copyright 2020 American Association for the Advancement of Science. (e) Illustration of the preparation of CNTs (above) and metal-confining CNT (M@CNT, below) via a CaC₂-mediated mechanism. (f) TEM images of Sn@CNTs. HAADF-STEM image and the corresponding elemental mappings of (g) Sn@CNT, (h) Zn@CNT, and (i) Fe@CNT. Reprinted with permission from ref 35. Copyright 2023 Wiley-VCH GmbH.

ı

tures.⁶⁷ This observed uniformity can be attributed to the significant presence of ${\rm CO_3}^{2-}$ ions within the molten medium. The swift nucleation of carbon on the W electrode, induced by the applied voltage, effectively diminishes the substantial impact of the ${\rm CO_3}^{2-}$ ion concentration on the resultant carbon morphology. Such spherical carbon particles with a small surface area of 120 m² g¹ delivered only a low specific capacitance of 318 mAh g¹¹ (50 mA g¹¹). However, the asprepared ${\rm CO_2\text{-}C}$ can transform into a hollow carbon sphere with an enlarged SSA of 400 m² g¹¹ in molten LiCl–KCl–2

mol % $CaCO_3$, which displayed a higher specific capacity of 550 mAh g^{-1} .⁶⁸

In addition, in molten $\rm Li_2CO_3$ – $\rm Li_2O$ (4 M $\rm Li_2O$ in $\rm Li_2CO_3$), a typical carbon material, CNTs with a productivity of 80–100% were successfully synthesized using a Ni anode and a steel cathode at 750 °C, which is quite different from most electrolytic irregular $\rm CO_2$ -C. ⁶⁹ In such an electrolysis system, anodic Ni is oxidized into Ni²⁺ and then transferred to the cathode, where it is reduced into metallic Ni to serve as nucleation sites for CNT growth. The presence of $\rm Li_2O$ in the melt can facilitate the transformation of straight CNTs into

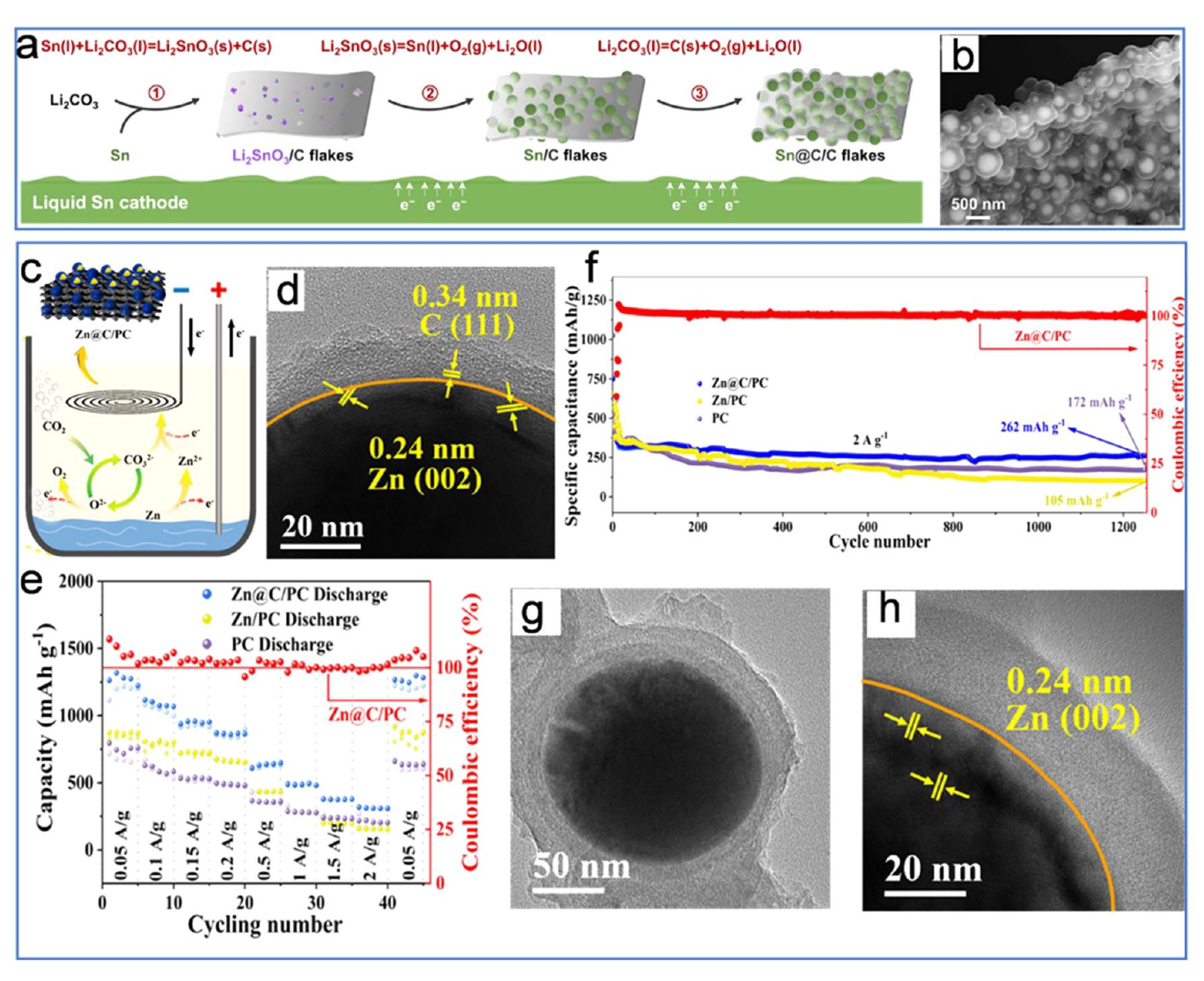


Figure 6. (a) Diagram showing Sn@C synthesis through a thermal–electrochemical reaction. (b) SEM image of the synthesized Sn@C/C flakes. Reprinted with permission from ref 72. Copyright 2023 Wiley-VCH GmbH. (c) Diagram depicting the synthesis process of Zn@C/PC. (d) HRTEM image of Zn@C/PC. (e) Rate and (f) cycling performances (at 2 A g⁻¹) of Zn@C/PC, Zn/PC, and PC electrodes. (g) TEM and (h) HRTEM images of Zn@C/PC after 1250 cycles. Reprinted with permission from ref 73. Copyright 2024 Elsevier.

tangled CNTs by introducing additional defects to the CNT structure (Figure 4a-c). The as-prepared tangled CNTs exhibit a diameter smaller than that of the straight CNTs (Figure 4d,e). Additionally, the higher I_D/I_G value indicates a greater number of defects in the tangled CNTs compared to the straight CNTs (Figure 4d,e). When the two types of CNTs are used as active materials for LIBs, the reversible capacity of the two types of CNTs during the second discharge cycle is approximately 370 mAh g⁻¹, which then settles to around 350 mAh g⁻¹ by the 15th cycle. However, distinct storage behaviors were observed between straight (less defective, $I_D/I_G = 0.4$) and tangled (more defective, $I_{\rm D}/I_{\rm G}$ = 0.9) CNTs. The capacity of straight CNTs remains consistent at approximately 360 mAh g⁻¹ throughout the cycling process. In contrast, the capacity of the tangled CNTs progressively increases, reaching around 460 mAh g⁻¹ after 200 cycles (Figure 4f-h). This difference suggests that the high defect content and complex structure of tangled CNTs might facilitate a transition from the typical dilute staging of Li⁺ in LiC₆ formation to a combination of this and a mechanism similar to pore filling. 70,71 Furthermore, it has been documented that carbon materials

rich in defects exhibit moderate sodium-ion (Na⁺) storage capacities, due to a synergistic mechanism that involves both intercalation and pore filling. The straight and tangled CNTs were used for SIBs due to their distinct defective degree. Tangled CNTs demonstrate reversible capacities over 130 mAh g⁻¹, which is about double that of straight CNTs, highlighting that defects in CNT materials are essential for Na⁺ storage. Moreover, they exhibit a higher capacity and excellent cycling stability compared with straight CNTs (Figure 4i–k). In another carbonate molten salt (Li₂CO₃:Na₂CO₃:K₂CO₃ = 43.5:31.5:25 mol %), the capacity of the as-prepared CO₂-C (amorphous carbon) exhibits a high reversible capacity of 798 mAh g⁻¹ (50 mA g⁻¹) because of the high SSA of 613.76 m² g⁻¹.

Based on the analysis above, enlarging the SSA and defective degree can increase the capacities of the CO₂-C to a certain extent. However, the specific capacities of metal-free CO₂-C are still far from practical application for LIBs. Recent scholarly endeavors have concentrated on integrating active metal elements such as Ge, Sn, Ni, and Zn into CO₂-derived carbons to fabricate metal/carbon composites, aiming to

augment the capacity performance in LIBs. 14,34,35,72,73 In particular, the technique of encapsulating high-capacity electrode materials within a carbonaceous matrix has been identified as an efficacious method to enhance the LIBs' performance. This approach effectively buffers volume alterations during the alloying and dealloying processes and ensures the structural integrity of the electrode, thereby significantly improving the cycling stability in LIBs. An amazing Ge@CNT was reported to enhance the overall LIBs performance by overcoming the intrinsic low-capacity characteristics of carbon.³⁴ In a GeO₂-containing molten NaCl-CaCl₂-CaO mixture, the initial reaction involves GeO₂ combining with ionized Ca²⁺ to yield a liquid CaGe alloy, serving as nucleation sites for the growth of CNTs. Concurrently, carbonate ions (CO₃²⁻), initially produced by capturing CO₂ with O²⁻, are reduced to CNTs and oxide ions (O²⁻), as shown in Figure 5a. As shown in Figure 5b, many Ge nanoparticles are embedded in the CNTs. When applied for LIBs, Ge@CNT exhibits a reversible capacity of 438 mAh g⁻¹ (5000 mA g⁻¹), outperforming the C-CNTs with a capacity of 29 mAh g⁻¹. At a low current density of 50 mA g⁻¹, the capacity of Ge@CNT can reach over 900 mAh g-1 (Figure 5c). Furthermore, its long-term stability is demonstrated by a retained capacity of 276 mAh g⁻¹ after 1000 cycles at 2000 mA g⁻¹, with a negligible average capacity decay rate of 0.04% per cycle (Figure 5d). The great improvement of Ge@CNTs compared to C-CNT can be attributed to the following four points: (1) The encapsulated Ge core delivers high Li⁺ storage capacities. (2) The CNT shell, with its significant free space, mitigates volume fluctuations during lithiation and delithiation, ensuring structural and mechanical stability. (3) The Li+permeable CNT sheath protects against Ge oxidation and the resultant GeO_x layer formation, which could hinder Li⁺ ion diffusion. (4) Ge nanoparticles are intimately connected to the CNT's inner walls, improving charge transfer and utilization of Ge atoms, thereby boosting the rate performance. By combining the unique properties of both the CNT sheath and the Ge core, we achieved a substantial enhancement in the overall performance of LIBs. In addition, other metal@CNTs, including Sn@CNTs, Zn@CNTs, and Fe@CNTs, were also synthesized, coupled with the reduction of CO_2 in molten salts. Nevertheless, the formation mechanisms of these three metal@ CNTs follow reaction processes different from the liquid metal nucleation mechanism. As shown in Figure 5e, the electrochemical reduction of CO₂ in a cost-effective, Ca-containing molten salt is depicted, efficiently producing CNTs and M@ CNTs via a CaC₂-mediated pathway.³⁵ In the synthesis of metal-free CNTs, CaCO3 in the melt is initially converted to CaC2, which then serves as the nucleation sites for CNT growth through the decomposition of CaCO₃, while the depleted CaCO₃ is replenished by the CaO and CO₂ cycle. In contrast, for the synthesis of metal@CNTs (Sn@CNTs, Zn@ CNTs, and Fe@CNTs), MO_x (metal oxides SnO₂, ZnO, and FeO) and CaCO3 are coreduced to liquid metals and CNTs, respectively, with the liquid metals embedded in the inner spaces of CNTs (Figure 5f-i). Sn@CNT, benefiting from the synergistic interaction between the Sn core and the CNT shell, exhibits a high capacity of 510 mAh g⁻¹ at a current of 1000 mA g⁻¹. These processes exemplify a strategic use of molten salt for CO2 capture and conversion, contributing to the development of innovative CNT composites and highlighting the adaptability of this technique in producing diverse CO₂derived carbon-based nanomaterials.

In the Ge@CNTs system, the liquid CaSn alloy acts as the nucleation site for CNT growth, which may provide insights for future research. Subsequent studies have expanded on this concept, specifically exploring liquid metal electrodes with a focus on the liquid forms of Sn and Zn. For example, in a carbonate molten salt medium, a liquid Sn cathode can be employed to synthesize Sn@C for LIBs. This synthesis process is distinct from that of the CaGe liquid. A thermal reaction between liquid Sn and molten Li₂CO₃ spontaneously forms the Li₂SnO₃ intermediate (Figure 6a).⁷² The decomposition voltages of Li₂SnO₃ (to Li₂O and Sn, at 1.99 V) and Li₂CO₃ (to Li₂O and C₁ at 1.30 V) are both lower than that of Li₂O (to Li, at 2.43 V), which facilitates the simultaneous generation of Sn and C while precluding the deposition of Li. Although Sn@ C/C flakes were obtained (Figure 6b), their capacity for LIBs is inferior compared to that of Sn@CNTs.35 Different from the liquid metal cathode where the reduction reaction takes place, Zn was reported as a liquid anode in molten salt to synthesize Zn@C/PC for ZIBs.⁷³ As illustrated in Figure 6c, during electrolysis in molten carbonates, Zn2+ ions are generated at the Zn anode/electrolyte interface through the oxidation of Zn and subsequently reduced with CO₃²⁻ to form Zn@C/PC (Figure 6d). This involves the concurrent oxidation of Zn to Zn²⁺ and the reduction of CO₃²⁻ to C and O²⁻. The in situproduced Zn²⁺ ions migrate to the cathode, where they are reduced, forming Zn@C, while O2- undergoes oxidation to O₂. Simultaneously, excess O²⁻ facilitates CO₂ capture to regenerate CO₃²⁻. Thus, the overall reaction transforms Zn and CO_2 to the carbon composite Zn@C/PC. The resultant Zn@C/PC demonstrates a high reversible capacity of 1271 mAh g⁻¹ at 50 mA g⁻¹ (Figure 6e) and sustains 81.4% of its capacity after 1250 cycles at 2 A g⁻¹ (Figure 6f). After extensive charge-discharge cycles, the integrity of the Zn@C core-shell structure is preserved, underscoring the exceptional stability of the Zn@C structure (Figure 6g,h). Notably, the Zn@C/PC composite exhibits a higher capacity and better cycling stability compared to the metal-free carbon and the mixture of C and Zn powder, implying that the synergistic effect of the Zn core and C shell facilitates the overall performance of the ZIBs. Additionally, liquid Zn was also used as a cathode to fabricate Zn@C via the heterogeneous nucleation of C on the liquid Zn droplets.74 When utilized in AlIBs, Zn@C maintains a capacity of approximately 90 mAh g⁻¹ after 450 cycles, whereas the capacity of hollow carbon (without a Zn core) dramatically drops to 30 mAh g⁻¹ at 200 mA g⁻¹. Those optimized metal/C composites increase the variety of electrolytic CO2-C, enlarge the capacity for ZIBs to a certain extent, and extend the application for batteries. However, its performance requires further enhancement, and the exploration of its applications remains at an early stage.

3.3. Electrocatalysts. Carbon-based nanomaterials have been widely used as electrocatalysts due to their good conductivity, chemical stability, excellent resistance to acid/alkaline solution, and modifiability, for example, the ORR, OER, and HER. The Nanocarbons with different dopants can show distinct electrochemical activities toward different reactions. Many works have confirmed that oxygen-doped carbon (O-C) displayed excellent 2e ORR activity. The oxygen functional groups (oxhydryl, carboxyl, and carbonyl) in the OC play a vital role in catalyzing the 2e ORR by modifying the reaction coordination. In addition, the intrinsic defects, for example, edges, topological defects, and vacancies, in nanocarbons also display the catalytic activity to the 2e ORR. The Toronton of the catalytic activity to the 2e ORR.

Table 3. Summary of CO₂-C-Based Nanomaterials for Electrocatalysts^a

product	electrolyte	electrolysis conditions	performance	year	app.	ref
CNTs-B ₂ O ₃ -300	$50 \text{ g of Li}_2\text{CO}_3 + 7 \text{ g of B}_2\text{O}_3$	770 °C, 300 mA cm $^{-2}$ for 1 h, anode = Ni, cathode = steel	H ₂ O ₂ selectivity: 83.42%	2021	2e ORR	11
DSPC0.5-5	Li ₂ CO ₃ -Na ₂ CO ₃ -K ₂ CO ₃ (30.5:11:8.5 wt %)	electrolysis I: 580 °C, anode = Ni, cathode = steel, 4 A $$ $$ $$ $$ $$ $$ $$ $$ selectivity: over 90% for 0.5 h	H ₂ O ₂ selectivity: over 90%	2022	2e ORR	13
		electrolysis II: 580 °C, anode = C, cathode = Ni, 0.5 A for 5 min				
Fe/Fe ₃ C-MC	Li ₂ CO ₃ -Na ₂ CO ₃ -K ₂ CO ₃ (41:34:25 mol %)	600 °C, 2.2 V for 9 h, anode = SnO ₂ , cathode = Fe ₂ O ₃ η_{10} = 320 mV, 1 M KOH pellet	$\eta_{10} = 320 \text{ mV}, 1 \text{ M KOH}$	2020	OER	37
NiCo@g-C	Li ₂ CO ₃ -Na ₂ CO ₃ -K ₂ CO ₃ (43.5:31.5:25 mol %)	580 °C, 2.1 V, anode = Ni ₁₁ Fe ₁₀ Cu, cathode = NiO and Co ₃ O ₄ (3:1 molar ratio)	$\eta_{10} = 195 \text{ mV}, 1 \text{ M KOH}$	2020	HER	101
Mo_2C film	Li ₂ CO ₃	900 °C, 3.1 V for 1 h, anode = NiCr alloy, cathode = Mo $~\eta_{10}=149~{\rm mV},~0.5~{\rm M~H_2SO_4}$ plate	$\eta_{10} = 149 \text{ mV}, 0.5 \text{ M H}_2 \text{SO}_4$	2021	HER	39
MoC-Mo ₂ C-790 electrode	Li ₂ CO ₃ -K ₂ CO ₃ (1:1 mol %)	790 °C, 3.5 mA cm $^{-2}$ for 2 h, anode = Ni ₁₁ Fe ₁₀ Cu, cathode = Mo	0.5 M H ₂ SO ₄ : $\eta_{10} = 114$ mV, $\eta_{100} = 183$ mV, $\eta_{500} = 256$ mV	2021	HER	38
			1 M KOH: $\eta_{10} = 98.2 \text{ mV}$, $\eta_{500} = 292 \text{ mV}$			
MoC-Mo ₂ C nanosheet	$CaCl_2$ - CaO (2.93%)	850 $^{\circ}$ C, 2.5 V, anode = SnO ₂ , cathode = Mo foil	0.5 M H_2SO_4 : $\eta_{10} = 250.9 \text{ mV}$	2021	HER	91
$Ni-Mo_2C-0.67$	LiF–NaF–KF (5:1: 4 mol %) + 1.3 mol % $\rm K_2CO_3$ + 1.3 mol % $\rm Na_2MoO_4$	750-820 °C, 250 mA cm ⁻² for 1 h, anode = Mo, cathode = Ni plate	0.5 M H_2SO_4 : $\eta_{10} = 165 \text{ mV}$, $\eta_{100} = 214 \text{ mV}$	2022	HER	95
			1 M KOH: $\eta_{10} = 151$ mV, $\eta_{100} = 194$ mV			
self-standing $MoC-Mo_2C$ electrode	Li ₂ CO ₃ -K ₂ CO ₃ (1:1 mol %)	800 °C, 2 mA cm $^{-2}$ for 2 h, anode = Ni $_{\rm II}$ Fe $_{\rm IO}$ Cu, cathode = Mo foil	3 M NaOH + 3 M NaCl at 85 °C: η_{500} = 179 mV	2023	HER	92
S-doped $lpha$ -MoC-550	${ m Li_2CO_3}~(20~{ m g}){ m -Na_2CO_3}~(20~{ m g}){ m -K_2CO_3}~(20~{ m g}){ m -MoO_3}~(20~{ m g}){ m -MoO_3}~($	580 °C, 0.5 A for 1 h, anode = graphite rod, cathode = steel	when current density is over 133 mA cm $^{-2}$, it is superior to 20% Pt/C	2023	HER	16
Ni-MoC-Mo ₂ C/Mo self- supported electrode	Li ₂ CO ₃ -K ₂ CO ₃ (62:38 mol %)	800 °C, 50 mA for 3 h, anode = Ni, cathode = Mo	1 M KOH: $\eta_{10} = 35 \text{ mV}$, $\eta_{100} = 113 \text{ mV}$	2023	HER	93
			0.5 M H_2SO_4 : $\eta_{10} = 73$ mV, $\eta_{100} = 153$ mV			
C_{60} -MoC-600	$\text{Li}_2\text{CO}_3 - \text{K}_2\text{CO}_3$	600 $^{\circ}$ C, 50 mA for 2 h, anode = Ni, cathode = Mo	1 M KOH: $\eta_{220} = 142 \text{ mV}$	2023	HER	94
^a app.: application. $\eta_{x} = \text{over}$	"app.: application. η_{ν} = overpotential, where x represents the current density (mA cm ⁻²)	$(mA cm^{-2}).$				

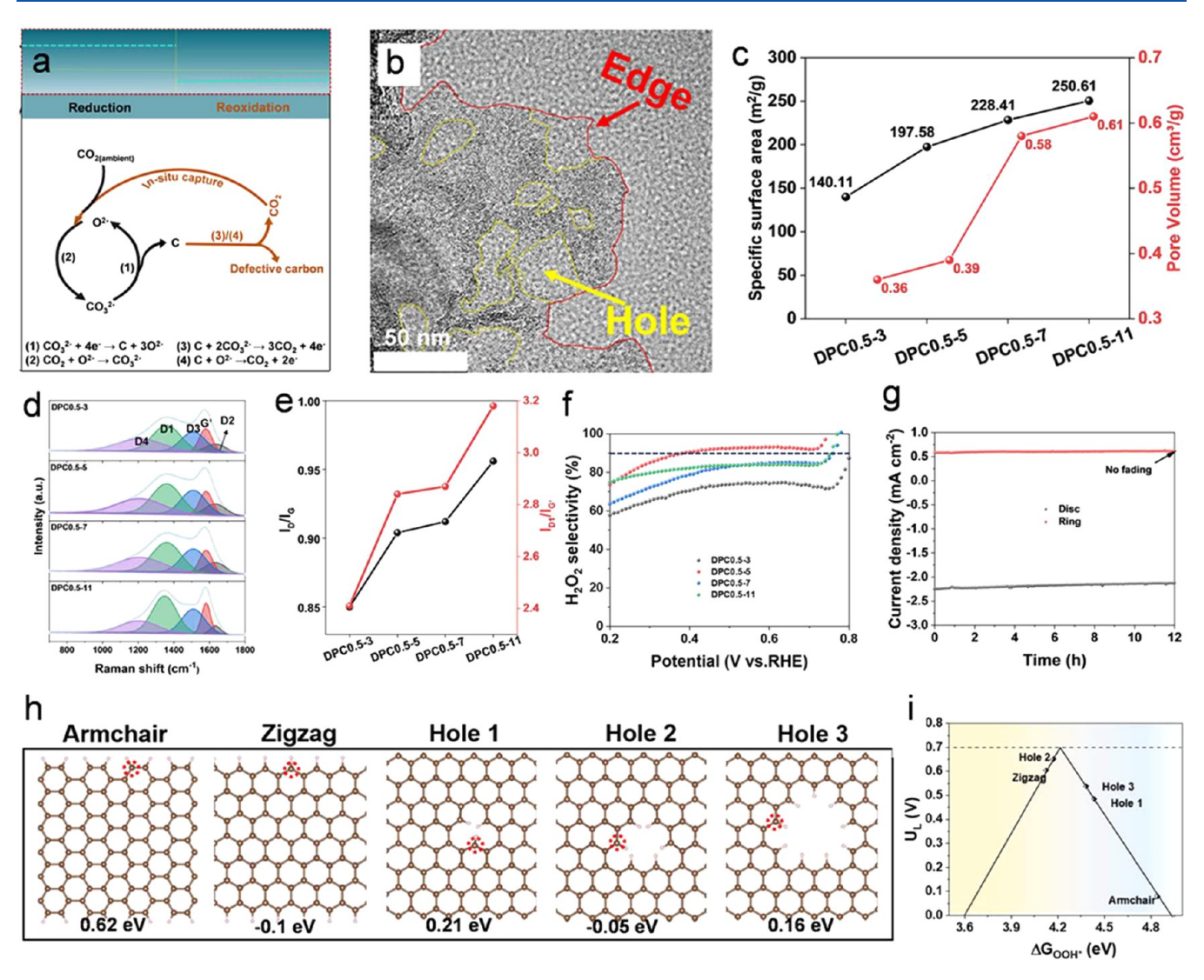


Figure 7. (a) Schematic illustration of the synthesis of DPCs by electrochemical reduction—reoxidation of CO₂ in molten salts. (b) TEM image of DPC0.5-5 (reoxidation for 5 min at 0.5 A). (c) SSA and pore volume of DPC0.5-x, where x represents a different time (min). 0.5 means the reoxidation current: 0.5 A. (d) Raman spectra, (e) $I_{\rm D}/I_{\rm G}$ and $I_{\rm D1}/I_{\rm G}$ values, and (f) H_2O_2 selectivity of DPC0.5-x. (g) i-t curves of DPC0.5-5 at a selected voltage of 0.5 V_{RHE}. (h) Various types of defects and site configurations and (i) the corresponding volcano plots for the 2e ORR (displayed with the limiting potential plotted as a function of $\Delta G_{\text{OOH}*}$). Reprinted with permission from ref 13. Copyright 2022 Elsevier.

Furthermore, when highly active metal elements are introduced to a carbonaceous matrix, the catalytic activity can be greatly enhanced. 85,86

The electrocatalytic applications of CO2-C-based nanomaterials have been limited and have only recently begun to be researched. Currently, they primarily include the 2e ORR, OER, and HER, as reported in recent studies (Table 3). Electrolytic CO₂-C originated from an oxygen-rich medium and inevitably contains O element, which implies their potential application for the 2e ORR. For example, the CO₂derived CNTs can be directly used as active materials for the 2e ORR due to the controllable oxygen content and various oxygen functional groups.¹¹ In addition, in a molten salt electrolytic system, the nanocarbons can be obtained through the reduction of CO2; however, the directly obtained nanocarbons probably exhibit a poor catalytic performance, as expected. Further modification of the nanocarbons has garnered significant attention from researchers. Anodic oxidation of CO₂-C has been confirmed as an effective strategy for enhancing the performance of the 2e ORR.¹³ After CO₂-C

is deposited on the cathode, its subsequent oxidation (oxidation current = 0.5 A) in molten salt can in situ create defects in the matrix of CO₂-C, thus forming defective porous carbon (DPC) through partial carbon reactions with CO₃²⁻ (C + $2\text{CO}_3^{2-} \rightarrow 3\text{CO}_2 + 4\text{e}^-$) and dissolved O^{2-} (C + $2O^{2-} \rightarrow \text{CO}_2 + 4\text{e}^-$) (Figure 7a).¹³ The thus-obtained DPC was confirmed to have abundant holes and rough edges, the SSA of which is also increased with the prolonging of the oxidation time (Figure 7b,c). Notably, due to the prolonged oxidation time, the D1 band, which represents the exposed edge defects on the graphene layers, is significantly enhanced. This leads to an increased area ratio of the D1 to G' band (denoted as $I_{\rm D1}/$ $I_{G'}$). The increase in both the I_D/I_G and $I_{D1}/I_{G'}$ ratios indicates the enhanced defective degree of the DPCs (Figure 7d,e). The sample DPC0.5-5 with a proper defective degree exhibits the highest H₂O₂ selectivity of over 90% and excellent stability, as shown in Figure 7f,g. The DFT calculations in Figure 7h,i demonstrate that the hole 2-type defect, closest to the top point of the volcano plot, exhibits the best catalytic activity to the 2e ORR. The metal-free CO₂-C unequivocally confirms its

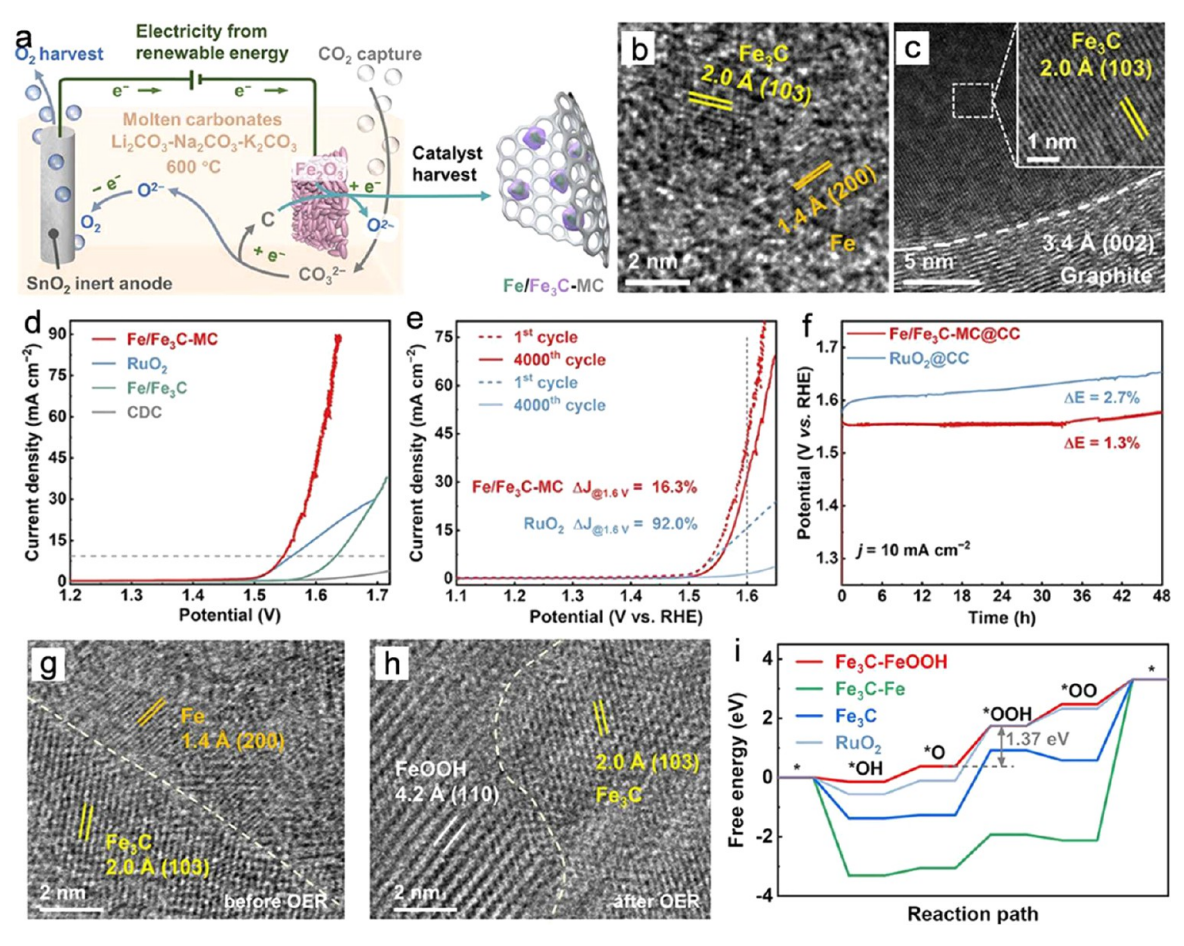


Figure 8. (a) Illustration of the simultaneous electrochemical reduction of Fe_2O_3 and CO_2 to Fe/Fe_3C -MC. (b and c) HRTEM images of Fe/Fe_3C -MC. (d) Linear-sweep voltammetry (LSV) curves and (e) LSV curves after 4000 cycles of Fe/Fe_3C -MC, Fe/Fe_3C , CDC, and RuO_2 . (f) Voltage—time curves recorded at 10 cm^{-2} . HRTEM images of the Fe/Fe_3C -MC catalyst (g) before and (h) after electrolysis at 10 mA cm^{-2} for 48 h. (i) Free energy curves for the OER on the Fe_3C -FeOOH, Fe_3C -Fe, Fe_3C , and RuO_2 models. CDC: CO_2 -derived carbon without Fe. Reprinted with permission from ref 37. Copyright 2020 Wiley-VCH GmbH.

significant potential as an electrocatalyst. However, the use of metal-free CO_2 -C in the ORR is still infrequently reported, likely due to the challenges in synthesizing N/metal-doped CO_2 -C, which facilitates the ORR performance.

To promote the electrocatalytic activity and explore additional applications of CO2-C, active metallic elements are introduced into CO₂-C to create metal/carbon composites using two strategies: (1) employing a cathode specially designed with active metals and (2) adding active metallic elements directly to the molten salt. During the synthesis of CO₂-derived metal/carbon composites, the process typically involves a coreduction of CO₂ and high-valence-state metallic elements or a combination of electroreduction and thermochemical reactions in the molten salt. In a typical example, a prefabricated Fe₂O₃ pellet serves as the cathode, with inert SnO₂ functioning as the anode, for synthesizing Fe/Fe₃Cmodified carbon (Fe/Fe₃C-MC).³⁷ During the electrolytic process, injected CO2 is reduced to C and O2, while Fe2O3 is concurrently reduced to metallic Fe, as shown in Figure 8a. The carbon matrix derived from CO₂ plays a crucial role in preventing the agglomeration of Fe species, thereby ensuring maximal exposure of the active Fe-C sites. Furthermore, the diffusion of C into the Fe core facilitates the gradual formation of Fe₃C, ultimately leading to elimination of the Fe/C interface and formation of the Fe₃C/C interface (Figure 8b,c). Fe/Fe₃C-MC showcases a notably low overpotential of $\eta_{10} = 320$ mV,

surpassing that of commercial RuO_2 (Figure 8d). Notably, Fe/Fe₃C-MC shows a lower current fading of 16.3% than that of RuO_2 (92%) at 1.6 V_{RHE} after 4000 cyclic voltammetry cycles (Figure 8e). Chronopotentiometry durability tests also further demonstrate the superior stability of Fe/Fe₃C-MC to RuO_2 during 48 h of electrolysis at 10 mA cm⁻² (Figure 8f). In the HRTEM images of Fe/Fe₃C-MC, it is observed that the initial Fe/Fe₃C interface undergoes a transformation into Fe₃C-FeOOH during the OER operation (Figure 8g,h). In addition, the DFT calculations demonstrate that the Fe₃C-FeOOH, Fe₃C-Fe, Fe₃C, and RuO_2 models exhibit energy barriers of 1.37, 5.43, 2.73, and 1.86 eV (Figure 8i), respectively, indicating that the in situ-generated FeOOH on Fe₃C is identified as the active site for the OER.

In addition to Fe/Fe₃C-MC used for the OER, other CO₂-derived carbon-based metal/carbon composites primarily include Mo-C materials, like MoC, Mo₂C, heteroatom-doped MoC or Mo₂C, and the composite of MoC and Mo₂C (Table 3). The synthesis of Mo-C materials typically includes the use of a Mo plate as an electrode or the addition of soluble Mo salts/oxides to the molten salt (Table 3). This process facilitates either the coreduction of CO₂ and Mo salts/oxides or the gradual thermochemical reaction between the reduced CO₂-C and Mo metal. The Mo plate is most commonly used as a cathode for preparing Mo-C composites. In a molten salt electrolysis system featuring such a Mo cathode, the CO₂-

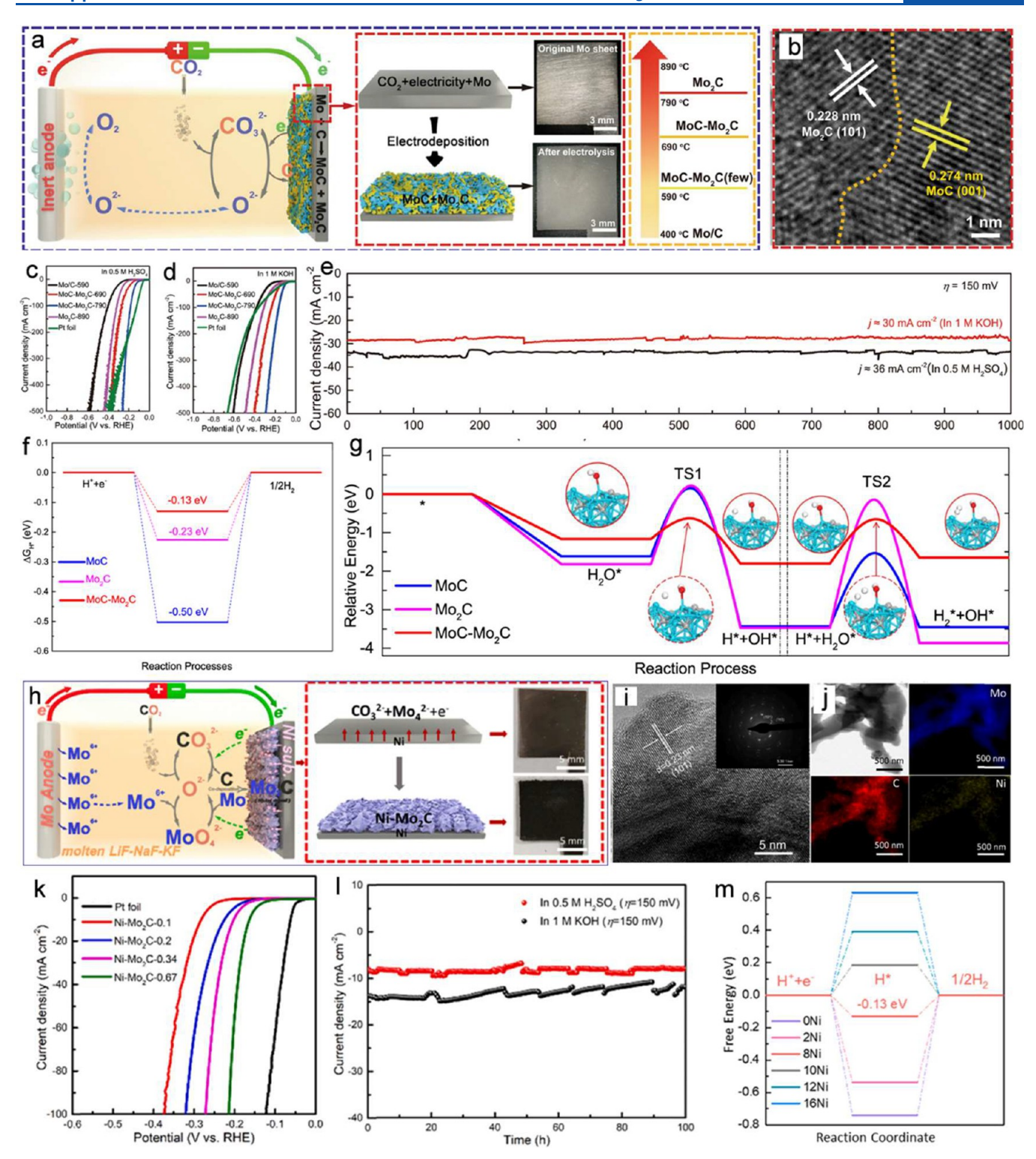


Figure 9. (a) Illustration of the synthesis of MoC-Mo₂C-790 in molten carbonate. (b) HRTEM image of MoC-Mo₂C-790. LSV curves of MoC-Mo₂C-790 in (c) 0.5 M H₂SO₄ and (d) 1 M KOH and (e) corresponding current density—time curves at an overpotential of 150 mV. (f) Calculated ΔG_{H^*} of the HER for the MoC, Mo₂C, and MoC-Mo₂C sites in an acid electrolyte at the equilibrium potential. (g) Calculated relative energy diagram of H₂O dissociation on the MoC, Mo₂C, and MoC-Mo₂C sites in an alkaline solution, TS: transition state. Reprinted with permission from ref 38. Copyright 2021 Springer Nature. (h) Illustration of the synthesis of Ni-Mo₂C-0.67 in molten LiF-NaF-KF. (i) TEM image and (j) corresponding elemental distributions. (k) LSV curves in 0.5 M H₂SO₄. (l) Current density—time curves at an overpotential of 150 mV of Ni-Mo₂C-0.67. (m) Calculated free-energy curves of the HER for xNi-Mo₂C (x = 0, 2, 8, 10, 12,and 16). Reprinted with permission from ref 95. Copyright 2022 Elsevier.

replenished ${\rm CO_3}^{2-}$ is initially reduced to solid carbon on the Mo surface. Subsequently, a carbiding reaction occurs between the electrolytic carbon and the Mo substrate, leading to the

formation of Mo_xC (x = 1 or 2). $^{38,39,91-94}$ Notably, the composition of synthetic Mo-C composites in molten carbonate is highly dependent on the reaction temperature

when employing a Mo plate as a cathode for electrolysis.³⁸ At 590 °C, only the reduction of CO₂ on the Mo surface occurs without any carbiding reaction, leading to the formation of Mo-C. As the temperature increases, MoC and Mo₂C begin to form, with higher temperatures promoting more Mo₂C formation in the resulting composites. When the temperature increases to 890 °C, exclusively Mo₂C is produced on the Mo cathode (Figure 9a). The MoC-Mo₂C-790 sample, synthesized at 790 °C, comprises a mixture of MoC and Mo₂C, forming a heterojunction between the MoC(001) and Mo₂C(101) planes (Figure 9b). The MoC-Mo₂C-790 electrode demonstrates small overpotentials of η_{10} = 114 mV and η_{100} = 183 mV in 0.5 M H_2SO_4 and η_{10} = 98.2 mV and η_{100} = 292 mV in 1 M KOH (Figure 9c,d). Additionally, the MoC-Mo₂C-790 electrode exhibits remarkable stability, maintaining a nearly constant catalytic current over 1000 h (totaling 2000 h for the same electrode) at an overpotential of 150 mV in both 0.5 M H₂SO₄ and 1 M KOH (Figure 9e). The DFT calculations indicate that the MoC-Mo₂C heterojunction displays the optimum Gibbs free energy of H* adsorption ($\Delta G_{H^*} = -0.13$ eV) in acidic conditions (Figure 9f). In an alkaline solution, the adsorption and intermediate states for hydrogen (H*), hydroxyl (OH*), and water (H₂O*) indicate the energetic favorability of various surface reactions on MoC, Mo2C, and MoC-Mo₂C. The MoC-Mo₂C composite appears to have the lowest energy barriers, suggesting a more efficient catalytic process compared to the single-phase MoC or Mo₂C catalysts (Figure 9g).

In contrast to employing Mo metal as the cathode for the synthesis of a Mo-C composite, using Mo salts/oxides as Mo sources to prepare a Mo-C composite undergoes distinct procedures. In molten LiF-NaF-KF (5:1:4 mol %) + 1.3 mol % K₂CO₃, Na₂MoO₄ was directly added to the melt to provide a Mo source. As shown in Figure 9h, the CO₂-replenished CO₃²⁻ is reduced to carbon on the Ni cathode coupled with the liberation of the oxidized O^{2-} ($O^{2-} + CO_2 = CO_3^{2-}$ and $CO_3^{2-} + 4e^- = C + 3O^{2-}$). Notably, the electroreduction of MoO₄²⁻ follows a pathway similar to that of CO₃²⁻, which is reduced to metallic Mo while releasing O2-. Meanwhile, anodic Mo is oxidized to Mo⁶⁺, which then combines with O²⁻ to generate MoO₄²⁻. The codeposition of Mo and C atoms on the cathode leads to the synthesis of Mo₂C. In addition, because of the deposition of Mo₂C taking place on the Ni cathode, the Ni atoms inevitably diffuse out and react with the Mo or C atoms, thus resulting in Ni-doped Mo₂C (Ni-Mo₂C; Figure 9i,j). The sample Ni-Mo₂C-0.67 with proper Ni content demonstrates a lower overpotential of η_{10} = 165 mV in 0.5 M H₂SO₄, which is superior to that of the previously reported Mo_2C-890 ($\eta_{10} = 220$ mV in 0.5 M H_2SO_4 ; Figure 9k). Furthermore, the current density-time curves for Ni-Mo₂C-0.67 display only slight fading after 100 h at $\eta = 150$ mV in both 0.5 M H₂SO₄ and 1 M KOH, demonstrating the excellent stability of Ni-Mo₂C-0.67. In addition, the DFT calculation indicates that different contents of Ni dopant in Mo₂C can optimize the HER free energy, thus enhancing the HER performance (Figure 9k). In addition to the Mo salt, Mo oxide (for example, MoO₃) can be directly used as a Mo feedstock to prepare a Mo-C composite in molten Li₂CO₃-Na₂CO₃-K₂CO₃. Upon the introduction of MoO₃ to the molten carbonate, it first converts to MoO₄²⁻ via reaction with CO₃²⁻ $(MoO_3 + CO_3^{2-} \rightarrow MoO_4^{2-} + CO_2)$. Subsequently, the in situ-generated MoO₄²⁻ and CO₂-replenished CO₃²⁻ are coreduced at the cathode to form MoC.³⁸ Those results

indicated that MoO₄²⁻ in molten salt plays an irreplaceable role in synthesizing the Mo-C composite.

4. CONCLUSION AND PERSPECTIVE

In this paper, the advantages of electroreduction of CO₂ in molten salt, reaction mechanism, and applications in capacitors, batteries, and electrocatalysts for CO₂-C-based nanomaterials are systematically summarized. The progressive development has garnered considerable interest, covering a range of metal-free to metal-containing CO₂-C composites. Initially, almost all metal-free CO₂-C were used in capacitors and batteries. However, in the past 5 years, the development and utilization of metal-containing CO₂-C composites as electrocatalysts for the OER and HER have begun. Additionally, recently developed metal-containing CO₂-C composites have been found to exhibit superior capacitive performances in batteries compared to metal-free CO₂-C.

Although molten salt electrolysis offers significant promise for CO₂ sequestration and its conversion into highly functional carbon materials, the resulting CO₂-C-based nanomaterials are observed to have suboptimal performances in capacitive and battery applications, especially when compared with other active materials in these areas. Additionally, the application of these materials in electrocatalysis is largely limited to the 2e ORR, OER, and HER. It is noteworthy that a majority of these electrocatalysts are Mo-based and predominantly designed for the HER. This specificity significantly restricts the broader application of CO₂-C-based nanomaterials. Furthermore, although various morphologies of CO2-C, including nanoparticles, hollow carbon spheres, 2D carbon flakes, porous carbon, octahedral carbon, CNTs, etc., have been reported, the formation mechanisms of most of these carbon structures still lack direct evidence. This deficiency significantly impedes material design and its further applications. Moreover, concerning metal-containing CO₂-C composites, the coreduction and thermochemical reactions are considered to be the widely accepted synthesis mechanisms. However, direct observation of these reaction processes is still lacking. Consequently, a high-temperature in situ reaction device is likely to be effective in elucidating the reaction mechanisms that are crucial for the purposeful design of CO₂-C-based materials for further applications. For example, the in situ observation of carbon deposition under various electrolysis conditions as well as the formation of intermediates should be explored using techniques such as in situ SEM, XPS, or X-ray diffraction. This approach may help in precisely designing the structure and composition of the obtained carbons. Additionally, efforts should be made to develop metal-free carbon nanomaterials doped with nonmetallic heteroatoms beyond merely O and S. This strategy would enhance the performance of capacitors and batteries and broaden the application spectrum of electrocatalysts. Furthermore, it is necessary to explore other applications of metal-containing CO2-C composites in various electrochemical reactions, such as the ORR, CO₂RR, and nitrogen reduction reaction, by introducing other active metals like Cu and Mn. The development of technologies for the capture and conversion of CO2 is pivotal in establishing a decarbonized strategy that integrates with energy storage and conversion applications, thereby ensuring a reduced carbon footprint.

AUTHOR INFORMATION

Corresponding Author

Yang Yang — NanoScience Technology Center, Department of Materials Science and Engineering, Renewable Energy and Chemical Transformation Cluster, Department of Chemistry, and The Stephen W. Hawking Center for Microgravity Research and Education, University of Central Florida, Orlando, Florida 32826, United States; occid.org/0000-0002-4410-6021; Email: Yang, Yang@ucf.edu

Authors

Ao Yu — NanoScience Technology Center, University of Central Florida, Orlando, Florida 32826, United States;
orcid.org/0000-0003-1449-6329

Shengwen Liu — NanoScience Technology Center, University of Central Florida, Orlando, Florida 32826, United States Wei Zhang — NanoScience Technology Center and Department of Materials Science and Engineering, University of Central Florida, Orlando, Florida 32826, United States; orcid.org/0000-0002-7846-8063

Complete contact information is available at: https://pubs.acs.org/10.1021/acsanm.4c00010

Author Contributions

A.Y.: writing—original draft. S.L. and W.Z.: review and editing. Y.Y.: supervision, funding acquisition, and project administration.

Notes

The authors declare no competing financial interest.

ACKNOWLEDGMENTS

Y.Y. acknowledges financial support from the National Science Foundation under Grant CBET-1949840 and ACS PRF (65481-ND10). A.Y. acknowledges financial support from the Preeminent Postdoctoral Program (P3) at UCF.

■ REFERENCES

- (1) Zhang, W.; Jin, Z.; Chen, Z. Rational-Designed Principles for Electrochemical and Photoelectrochemical Upgrading of CO_2 to Value-Added Chemicals. *Adv. Sci.* **2022**, *9*, No. 2105204.
- (2) Peng, P.; Yu, A.; Ren, J. W.; Li, F. F. Electrolytic Carbons from CO₂ and Their Applications. *ES Energy Environ.* **2018**, 2, 9–20.
- (3) Li, F.-F.; Lau, J.; Licht, S. Sungas instead of syngas: efficient coproduction of CO and H₂ with a single beam of sunlight. *Adv. Sci.* **2015**, 2, No. 1500260.
- (4) Matsuura, F.; Wakamatsu, T.; Natsui, S.; Kikuchi, T.; Suzuki, R. O. CO Gas Production by Molten Salt Electrolysis from CO₂ Gas. *ISIJ. Int.* **2015**, *55*, 404–408.
- (5) Lv, C.; Zhong, L.; Liu, H.; Fang, Z.; Yan, C.; Chen, M.; Kong, Y.; Lee, C.; Liu, D.; Li, S.; Liu, J.; Song, L.; Chen, G.; Yan, Q.; Yu, G. Selective electrocatalytic synthesis of urea with nitrate and carbon dioxide. *Nat. Sustain.* **2021**, *4*, 868–876.
- (6) Jiang, M.; Zhu, M.; Wang, M.; He, Y.; Luo, X.; Wu, C.; Zhang, L.; Jin, Z. Review on Electrocatalytic Coreduction of Carbon Dioxide and Nitrogenous Species for Urea Synthesis. *ACS Nano* **2023**, *17*, 3209–3224.
- (7) Wu, Y.; Jiang, Z.; Lin, Z.; Liang, Y.; Wang, H. Direct electrosynthesis of methylamine from carbon dioxide and nitrate. *Nat. Sustain.* **2021**, *4*, 725–730.
- (8) Zhang, W.; Yang, S.; Jiang, M.; Hu, Y.; Hu, C.; Zhang, X.; Jin, Z. Nanocapillarity and Nanoconfinement Effects of Pipet-like Bismuth@ Carbon Nanotubes for Highly Efficient Electrocatalytic CO₂ Reduction. *Nano Lett.* **2021**, *21*, 2650–2657.
- (9) Yang, S.; Jiang, M.; Zhang, W.; Hu, Y.; Liang, J.; Wang, Y.; Tie, Z.; Jin, Z. In Situ Structure Refactoring of Bismuth Nanoflowers for

- Highly Selective Electrochemical Reduction of CO_2 to Formate. *Adv. Funct. Mater.* **2023**, 33, No. 2301984.
- (10) Jiang, M.; Zhu, M.; Wang, H.; Song, X.; Liang, J.; Lin, D.; Li, C.; Cui, J.; Li, F.; Zhang, X. L.; Tie, Z.; Jin, Z. Rapid and Green Electric-Explosion Preparation of Spherical Indium Nanocrystals with Abundant Metal Defects for Highly-Selective CO₂ Electroreduction. *Nano Lett.* **2023**, 23, 291–297.
- (11) Yu, A.; Ma, G.; Zhu, L.; Hu, Y.; Zhang, R.; Hsu, H.-Y.; Peng, P.; Li, F.-F. Electrochemically controlled in situ conversion of CO₂ to defective carbon nanotubes for enhanced H₂O₂ production. *Nanoscale* **2021**, *13*, 15973–15980.
- (12) Yu, A.; Ma, G.; Jiang, J.; Hu, Y.; Su, M.; Long, W.; Gao, S.; Hsu, H.-Y.; Peng, P.; Li, F.-F. Bio-inspired and eco-friendly synthesis of 3D spongy meso-microporous carbons from CO₂ for supercapacitors. *Chem. Eur. J.* **2021**, 27, 10405–10412.
- (13) Yu, A.; Ma, G.; Zhu, L.; Zhang, R.; Li, Y.; Yang, S.; Hsu, H.-Y.; Peng, P.; Li, F.-F. Conversion of CO₂ to defective porous carbons in one electro-redox cycle for boosting electrocatalytic H₂O₂ production. *Appl. Catal., B* **2022**, *307*, No. 121161.
- (14) Yu, A.; Zhao, Y.; Zhu, L.; Yang, W.; Peng, P.; Li, F.-F. In-situ Ni-oxidation-assisted coupling reduction of NiO and CO_2 to synthesize core-shell Ni@octahedral carbon with energy storage properties. *Chem. Eng. J.* **2023**, *462*, No. 142268.
- (15) Yu, A.; Zhao, Y.; Zhang, W.; Yang, W.; Zhu, L.; Peng, P.; Li, F.-F.; Yang, Y. Bi-Directional Electrolytic Reduction of CO_2 to Mesoporous Carbons with Regulated Structure and Surface Functional Groups for Zn-ion Capacitors. *Adv. Funct. Mater.* **2024**, *34*, No. 2309666.
- (16) Zhu, L.; Zhao, Y.; Yang, W.; Hsu, H.-Y.; Peng, P.; Li, F.-F. Low-temperature selective synthesis of metastable α -MoC with electrochemical properties: Electrochemical co-reduction of CO_2 and MoO_3 in molten salts. *Chin. Chem. Lett.* **2024**, *35*, No. 108583.
- (17) 20 Years of Carbon Capture and Storage; International Energy Agency, 2016.
- (18) Zhu, Q.; Zeng, Y.; Zheng, Y. Overview of CO₂ capture and electrolysis technology in molten salts: operational parameters and their effects. *Ind. Chem. Mater.* **2023**, *1*, 595–617.
- (19) Jiang, R.; Gao, M.; Mao, X.; Wang, D. Advancements and potentials of molten salt CO₂ capture and electrochemical transformation (MSCC-ET) process. *Curr. Opin. Electrochem.* **2019**, *17*, 38–46.
- (20) Xiao, W.; Wang, D. The electrochemical reduction processes of solid compounds in high temperature molten salts. *Chem. Soc. Rev.* **2014**, *43*, 3215–3228.
- (21) Weng, W.; Tang, L. Z.; Xiao, W. Capture and electro-splitting of CO₂ in molten salts. *J. Energy Chem.* **2019**, *28*, 128–143.
- (22) Pletcher, D. The cathodic reduction of carbon dioxide—What can it realistically achieve? A mini review. *Electrochem. Commun.* **2015**, *61*, 97–101.
- (23) Li, K.; An, X.; Park, K. H.; Khraisheh, M.; Tang, J. A critical review of CO_2 photoconversion: Catalysts and reactors. *Catal. Today* **2014**, 224, 3–12.
- (24) Weng, W.; Tang, L.; Xiao, W. Capture and electro-splitting of CO₂ in molten salts. *J. Energy Chem.* **2019**, 28, 128–143.
- (25) García de Arquer, F. P.; Dinh, C.-T.; Ozden, A.; Wicks, J.; McCallum, C.; Kirmani, A. R.; Nam, D.-H.; Gabardo, C.; Seifitokaldani, A.; Wang, X.; Li, Y. C.; Li, F.; Edwards, J.; Richter, L. J.; Thorpe, S. J.; Sinton, D.; Sargent, E. H. CO₂ electrolysis to multicarbon products at activities greater than 1 A cm⁻². *Science* **2020**, 367, 661–666.
- (26) Li, Z.; Zhang, L.; Nishiura, M.; Luo, G.; Luo, Y.; Hou, Z. CO₂ Activation by Lewis Pairs Generated Under Copper Catalysis Enables Difunctionalization of Imines. *J. Am. Chem. Soc.* **2020**, *142*, 1966–1974
- (27) Wei, L.; Li, H.; Chen, J.; Yuan, Z.; Huang, Q.; Liao, X.; Henkelman, G.; Chen, Y. Thiocyanate-Modified Silver Nanofoam for Efficient CO2 Reduction to CO. ACS Catal. 2020, 10, 1444–1453.
- (28) Cao, J.-P.; Xue, Y.-S.; Li, N.-F.; Gong, J.-J.; Kang, R.-K.; Xu, Y. Lewis Acid Dominant Windmill-Shaped V8 Clusters: A Bifunctional

- Heterogeneous Catalyst for CO₂ Cycloaddition and Oxidation of Sulfides. J. Am. Chem. Soc. **2019**, 141, 19487–19497.
- (29) Chu, W.-Y.; Culakova, Z.; Wang, B. T.; Goldberg, K. I. Acid-assisted hydrogenation of CO₂ to methanol in a homogeneous catalytic cascade system. *ACS Catal.* **2019**, *9*, 9317–9326.
- (30) Wang, T.; Zhang, Q.; Lian, K.; Qi, G.; Liu, Q.; Feng, L.; Hu, G.; Luo, J.; Liu, X. Fe nanoparticles confined by multiple-heteroatom-doped carbon frameworks for aqueous Zn-air battery driving CO₂ electrolysis. *J. Colloid Interface Sci.* **2024**, *655*, 176–186.
- (31) Gao, S.; Chen, S.; Liu, Q.; Zhang, S.; Qi, G.; Luo, J.; Liu, X. Bifunctional BiPd Alloy Particles Anchored on Carbon Matrix for Reversible Zn–CO₂ Battery. ACS Applied Nano Materials **2022**, 5, 12387–12394.
- (32) Wang, X.; Liu, S.; Zhang, H.; Zhang, S.; Meng, G.; Liu, Q.; Sun, Z.; Luo, J.; Liu, X. Polycrystalline SnSx nanofilm enables CO₂ electroreduction to formate with high current density. *Chem. Commun.* **2022**, 58, 7654–7657.
- (33) Bara, J. E.; Camper, D. E.; Gin, D. L.; Noble, R. D. Room-Temperature Ionic Liquids and Composite Materials: Platform Technologies for CO2 Capture. *Acc. Chem. Res.* **2010**, *43*, 152–159.
- (34) Weng, W.; Jiang, B.; Wang, Z.; Xiao, W. In situ electrochemical conversion of CO₂ in molten salts to advanced energy materials with reduced carbon emissions. *Sci. Adv.* **2020**, *6*, No. eaay9278.
- (35) Cao, J.; Jing, S.; Wang, H.; Xu, W.; Zhang, M.; Xiao, J.; Peng, Y.; Ning, X.; Wang, Z.; Xiao, W. Pure and Metal-confining Carbon Nanotubes through Electrochemical Reduction of Carbon Dioxide in Ca-based Molten Salts. *Angew. Chem., Int. Ed.* **2023**, 62, No. e202306877.
- (36) Licht, S.; Liu, X.; Licht, G.; Wang, X.; Swesi, A.; Chan, Y. Amplified CO₂ reduction of greenhouse gas emissions with C2CNT carbon nanotube composites. *Materials Today Sustainability* **2019**, *6*, No. 100023
- (37) Liang, X.; Xiao, J.; Weng, W.; Xiao, W. Electrochemical Reduction of Carbon Dioxide and Iron Oxide in Molten Salts to Fe/Fe₃C Modified Carbon for Electrocatalytic Oxygen Evolution. *Angew. Chem., Int. Ed.* **2021**, *60*, 2120–2124.
- (38) Liu, W.; Wang, X.; Wang, F.; Du, K.; Zhang, Z.; Guo, Y.; Yin, H.; Wang, D. A durable and pH-universal self-standing MoC–Mo₂C heterojunction electrode for efficient hydrogen evolution reaction. *Nat. Commun.* **2021**, *12*, *6776*.
- (39) Xiao, H.; Zhu, H.; Weng, W.; Li, K.; Li, W.; Xiao, W. Electrochemical fixation of CO₂ over a Mo plate to prepare a Mo₂C film for electrocatalytic hydrogen evolution. *Mater. Chem. Front.* **2021**, 5, 4963–4969.
- (40) Yu, A.; Ma, G.; Ren, J.; Peng, P.; Li, F.-F. Sustainable carbons and fuels: recent advances of CO₂ conversion in molten salts. *ChemSusChem* **2020**, *13*, 6229–6245.
- (41) Claes, P.; Moyaux, D.; Peeters, D. Solubility and Solvation of Carbon Dioxide in the Molten Li₂CO₃/Na₂CO₃/K₂CO₃ (43.5:31.5:25.0 mol-%) Eutectic Mixture at 973 K I. Experimental Part. Eur. J. Inorg. Chem. 1999, 1999, 583–588.
- (42) Peeters, D.; Moyaux, D.; Claes, P. Solubility and Solvation of Carbon Dioxide in the Molten Li₂CO₃/Na₂CO₃/K₂CO₃ (43.5:31.5:25.0 mol-%) Eutectic Mixture at 973 K II. Theoretical Part. *Eur. J. Inorg. Chem.* **1999**, 1999, 589–592.
- (43) Licht, S.; Wang, B.; Wu, H. STEP—A Solar Chemical Process to End Anthropogenic Global Warming. II: Experimental Results. *J. Phys. Chem. C* 2011, *115*, 11803–11821.
- (44) Ren, J.; Licht, S. Tracking airborne CO₂ mitigation and low cost transformation into valuable carbon nanotubes. *Sci. Rep.* **2016**, *6*, 27760.
- (45) Deng, B.; Tang, J.; Mao, X.; Song, Y.; Zhu, H.; Xiao, W.; Wang, D. Kinetic and Thermodynamic Characterization of Enhanced Carbon Dioxide Absorption Process with Lithium Oxide-Containing Ternary Molten Carbonate. *Environ. Sci. Technol.* **2016**, *50*, 10588–10595.
- (46) Hu, L.; Jiao, S.; Song, Y.; Ge, J.; Zhu, J. Capture and electrochemical conversion of CO₂ to ultrathin graphite sheets in CaCl₂-based melts. *J. Mater. Chem. A* **2015**, *3*, 21211–21218.

- (47) Ren, J.; Li, F. F.; Lau, J.; Gonzãlez-Urbina, L.; Licht, S. One-pot synthesis of carbon nanofibers from CO₂. *Nano Lett.* **2015**, *15*, 6142–6148
- (48) Yin, H.; Mao, X.; Tang, D.; Xiao, W.; Xing, L.; Zhu, H.; Wang, D.; Sadoway, D. R. Capture and electrochemical conversion of CO₂ to value-added carbon and oxygen by molten salt electrolysis. *Energy Environ. Sci.* **2013**, *6*, 1538–1545.
- (49) Hu, L.; Deng, B.; Du, K.; Jiang, R.; Dou, Y.; Wang, D. Tunable Selectivity and High Efficiency of CO₂ Electroreduction via Borate-Enhanced Molten Salt Electrolysis. *iScience* **2020**, 23, No. 101607.
- (50) Chen, Z. G.; Deng, B. W.; Du, K. F.; Mao, X. H.; Zhu, H.; Xiao, W.; Wang, D. H. Flue-Gas-Derived Sulfur-Doped Carbon with Enhanced Capacitance. *Adv. Sustainable Syst.* **2017**, *1*, No. 1700047.
- (51) Tang, D.; Dou, Y.; Yin, H.; Mao, X.; Xiao, W.; Wang, D. The capacitive performances of carbon obtained from the electrolysis of CO₂ in molten carbonates: Effects of electrolysis voltage and temperature. *J. Energy Chem.* **2020**, *51*, 418–424.
- (52) Deng, B. W.; Mao, X. H.; Xiao, W.; Wang, D. H. Microbubble effect-assisted electrolytic synthesis of hollow carbon spheres from CO₂. J. Mater. Chem. A **2017**, *5*, 12822–12827.
- (53) Chen, Z.; Deng, B.; Du, K.; Mao, X.; Zhu, H.; Xiao, W.; Wang, D. Flue-Gas-Derived Sulfur-Doped Carbon with Enhanced Capacitance. *Adv. Sustainable Syst.* **2017**, *1*, No. 1700047.
- (54) Pan, Z.; Lu, Z.; Xu, L.; Wang, D. A robust 2D porous carbon nanoflake cathode for high energy-power density Zn-ion hybrid supercapacitor applications. *Appl. Surf. Sci.* **2020**, *510*, No. 145384.
- (55) Wang, H.; Ye, W.; Yang, Y.; Zhong, Y.; Hu, Y. Zn-ion hybrid supercapacitors: Achievements, challenges and future perspectives. *Nano Energy* **2021**, *85*, No. 105942.
- (56) Song, M.; Tan, H.; Chao, D.; Fan, H. J. Recent advances in Zn-Ion batteries. *Adv. Funct. Mater.* **2018**, 28, No. 1802564.
- (57) Li, C.; Xie, X.; Liang, S.; Zhou, J. Issues and future perspective on zinc metal anode for rechargeable aqueous zinc-ion batteries. *Energy Environ. Sci.* **2020**, *3*, 146–159.
- (58) Ming, J.; Guo, J.; Xia, C.; Wang, W.; Alshareef, H. N. Zinc-ion batteries: Materials, mechanisms, and applications. *Mater. Sci. Eng. R Rep.* **2019**, *135*, 58–84.
- (59) Liang, Y.; Wang, Y.; Mi, H.; Sun, L.; Ma, D.; Li, H.; He, C.; Zhang, P. Functionalized carbon nanofiber interlayer towards dendrite-free, Zn-ion batteries. *Chem. Eng. J.* **2021**, 425, No. 131862.
- (60) Zheng, Y.; Zhao, W.; Jia, D.; Liu, Y.; Cui, L.; Wei, D.; Zheng, R.; Liu, J. Porous carbon prepared via combustion and acid treatment as flexible zinc-ion capacitor electrode material. *Chem. Eng. J.* **2020**, 387, No. 124161.
- (61) Zhang, H.; Liu, Q.; Fang, Y.; Teng, C.; Liu, X.; Fang, P.; Tong, Y.; Lu, X. Boosting Zn-Ion Energy Storage Capability of Hierarchically Porous Carbon by Promoting Chemical Adsorption. *Adv. Mater.* **2019**, *31*, No. 1904948.
- (62) Zhang, D.; Li, L.; Gao, Y.; Wu, Y.; Deng, J. Carbon-Based Materials for a New Type of Zinc-Ion Capacitor. *ChemElectroChem.* **2021**, *8*, 1541–1557.
- (63) Jing, X.; Ma, Y.; Wang, F.; Li, W.; Wang, D. $\rm CO_2$ -Derived Oxygen-Rich Carbon with Enhanced Redox Reactions as a Cathode Material for Aqueous Zn-Ion Batteries. *ChemistrySelect* **2022**, 7, No. e202201133.
- (64) Lou, G.; Pei, G.; Wu, Y.; Lu, Y.; Wu, Y.; Zhu, X.; Pang, Y.; Shen, Z.; Wu, Q.; Fu, S.; Chen, H. Combustion conversion of wood to N, O co-doped 2D carbon nanosheets for zinc-ion hybrid supercapacitors. *Chem. Eng. J.* **2021**, *413*, No. 127502.
- (65) Chen, H.; Zheng, Y.; Zhu, X.; Hong, W.; Tong, Y.; Lu, Y.; Pei, G.; Pang, Y.; Shen, Z.; Guan, C. Bamboo-derived porous carbons for Zn-ion hybrid supercapacitors. *Mater. Res. Bull.* **2021**, *139*, No. 111281.
- (66) Zhou, L.; Cao, H.; Zhu, S.; Hou, L. R.; Yuan, C. Z. Hierarchical micro-mesoporous N- and O-enriched carbon derived from disposable. *Green Chem.* **2015**, *17*, 2373–2382.
- (67) Ge, J.; Hu, L.; Wang, W.; Jiao, H.; Jiao, S. Electrochemical Conversion of CO₂ into Negative Electrode Materials for Li-Ion Batteries. *ChemElectroChem.* **2015**, 2, 224–230.

- (68) Deng, B.; Tang, J.; Gao, M.; Mao, X.; Zhu, H.; Xiao, W.; Wang, D. Electrolytic synthesis of carbon from the captured CO₂ in molten LiCl–KCl–CaCO₃: Critical roles of electrode potential and temperature for hollow structure and lithium storage performance. *Electrochim. Acta* **2018**, 259, 975–985.
- (69) Licht, S.; Douglas, A.; Ren, J.; Carter, R.; Lefler, M.; Pint, C. L. Carbon Nanotubes Produced from Ambient Carbon Dioxide for Environmentally Sustainable Lithium-Ion and Sodium-Ion Battery Anodes. ACS Central Sci. 2016, 2, 162–8.
- (70) Inaba, M.; Yoshida, H.; Ogumi, Z.; Abe, T.; Mizutani, Y.; Asano, M. In Situ Raman Study on Electrochemical Li Intercalation into Graphite. *J. Electrochem. Soc.* **1995**, *142*, 20.
- (71) Bommier, C.; Surta, T. W.; Dolgos, M.; Ji, X. New Mechanistic Insights on Na-Ion Storage in Nongraphitizable Carbon. *Nano Lett.* **2015**, *15*, 5888–5892.
- (72) Jing, S.; Sheng, R.; Liang, X.; Gu, D.; Peng, Y.; Xiao, J.; Shen, Y.; Hu, D.; Xiao, W. Overall Carbon-neutral Electrochemical Reduction of CO2 in Molten Salts using a Liquid Metal Sn Cathode. *Angew. Chem., Int. Ed.* **2023**, *62*, No. e202216315.
- (73) Zhao, Y.; Yang, W.; Yu, A.; Peng, P.; Li, F.-F. Liquid Zn-Anode-Assisted molten salt electrolysis of CO₂ to synthesize Zn@C/PC for Lithium-Ion battery anode. *Appl. Surf. Sci.* **2024**, *649*, No. 159106.
- (74) Lv, T.; Xiao, J.; Weng, W.; Xiao, W. Electrochemical Fixation of Carbon Dioxide in Molten Salts on Liquid Zinc Cathode to Zinc@ Graphitic Carbon Spheres for Enhanced Energy Storage. *Adv. Energy Mater.* **2020**, *10*, No. 2002241.
- (75) Yu, A.; Peng, Z.; Li, Y.; Zhu, L.; Peng, P.; Li, F.-F. Fullerene-Derived Carbon Nanotubes and Their Electrocatalytic Properties in Oxygen Reduction and Zn-Air Batteries. *ACS Appl. Mater. Interfaces* **2022**, *14*, 42337–42346.
- (76) Yu, A.; Joshi, N.; Zhang, W.; Yang, Y. Advances in ORR, OER, and HER of fullerenes and derivatives: From DFT calculations to experimental identification. *Adv. Sensor Energy Mater.* **2023**, 2, No. 100061.
- (77) Yu, A.; Long, W.; Zhu, L.; Zhao, Y.; Peng, P.; Li, F.-F. Transformation of postsynthesized F-MOF to Fe/N/F-tridoped carbon nanotubes as oxygen reduction catalysts for high power density Zn-air batteries. *Chin. Chem. Lett.* **2023**, *34*, No. 107860.
- (78) Zhang, W.; Chang, J.; Yang, Y. Strong precious metal-metal oxide interaction for oxygen reduction reaction: A strategy for efficient catalyst design. *SusMat* **2023**, *3*, 2–20.
- (79) Lu, Z. Y.; Chen, G. X.; Siahrostami, S.; Chen, Z. H.; Liu, K.; Xie, J.; Liao, L.; Wu, T.; Lin, D. C.; Liu, Y.; Jaramillo, T. F.; Nørskov, J. K.; Cui, Y. High-efficiency oxygen reduction to hydrogen peroxide catalysed by oxidized carbon materials. *Nat. Catal.* **2018**, *1*, 156–162.
- (80) Han, L.; Sun, Y. Y.; Li, S.; Cheng, C.; Halbig, C. E.; Feicht, P.; Hübner, J. L.; Strasser, P.; Eigler, S. In-plane carbon lattice-defect regulating electrochemical oxygen reduction to hydrogen peroxide production over nitrogen-doped graphene. *ACS Catal.* **2019**, *9*, 1283–1288.
- (81) Melchionna, M.; Fornasiero, P.; Prato, M. The rise of hydrogen peroxide as the main product by metal-free catalysis in oxygen reductions. *Adv. Mater.* **2019**, *31*, No. e1802920.
- (82) Sa, Y. J.; Kim, J. H.; Joo, S. H. Active Edge-Site-Rich Carbon Nanocatalysts with Enhanced Electron Transfer for Efficient Electrochemical Hydrogen Peroxide Production. *Angew. Chem., Int. Ed. Engl.* **2019**, 58, 1100–1105.
- (83) Sheng, H.; Hermes, E. D.; Yang, X.; Ying, D.; Janes, A. N.; Li, W.; Schmidt, J. R.; Jin, S. Electrocatalytic production of H_2O_2 by selective oxygen reduction using earth-abundant cobalt pyrite CoS_2 . *ACS Catal.* **2019**, *9*, 8433–8442.
- (84) Zhu, J.; Xiao, X.; Zheng, K.; Li, F.; Ma, G.; Yao, H.-C.; Wang, X.; Chen, Y. KOH-treated reduced graphene oxide: 100% selectivity for H₂O₂ electroproduction. *Carbon* **2019**, *153*, 6–11.
- (85) Jung, E.; Shin, H.; Lee, B.-H.; Efremov, V.; Lee, S.; Lee, H. S.; Kim, J.; Hooch Antink, W.; Park, S.; Lee, K.-S.; Cho, S.-P.; Yoo, J. S.; Sung, Y.-E.; Hyeon, T. Atomic-level tuning of Co-N-C catalyst for high-performance electrochemical H_2O_2 production. *Nat. Mater.* **2020**, *19*, 436-442.

- (86) Shen, R.; Chen, W.; Peng, Q.; Lu, S.; Zheng, L.; Cao, X.; Wang, Y.; Zhu, W.; Zhang, J.; Zhuang, Z.; Chen, C.; Wang, D.; Li, Y. High-Concentration Single Atomic Pt Sites on Hollow CuSx for Selective O2 Reduction to H₂O₂ in Acid Solution. *Chem.* **2019**, *5*, 2099–2110.
- (87) Yuan, K.; Sfaelou, S.; Qiu, M.; Lützenkirchen-Hecht, D.; Zhuang, X.; Chen, Y.; Yuan, C.; Feng, X.; Scherf, U. Synergetic Contribution of Boron and Fe—Nx Species in Porous Carbons toward Efficient Electrocatalysts for Oxygen Reduction Reaction. *ACS Energy Letters* **2018**, 3, 252–260.
- (88) Han, J.; Meng, X.; Lu, L.; Bian, J.; Li, Z.; Sun, C. Single-Atom Fe-Nx-C as an Efficient Electrocatalyst for Zinc—Air Batteries. *Adv. Funct. Mater.* **2019**, 29, No. 1808872.
- (89) Han, M.; Shi, M.; Wang, J.; Zhang, M.; Yan, C.; Jiang, J.; Guo, S.; Sun, Z.; Guo, Z. Efficient bifunctional Co/N dual-doped carbon electrocatalysts for oxygen reduction and evolution reaction. *Carbon* **2019**, *153*, 575–584.
- (90) Wang, X.; Li, Z.; Qu, Y.; Yuan, T.; Wang, W.; Wu, Y.; Li, Y. Review of Metal Catalysts for Oxygen Reduction Reaction: From Nanoscale Engineering to Atomic Design. *Chem.* **2019**, *5*, 1486–1511
- (91) Chen, Y.; Gao, B.; Wang, M.; Xiao, X.; Lv, A.; Jiao, S.; Chu, P. K. Dual-phase MoC-Mo₂C nanosheets prepared by molten salt electrochemical conversion of CO₂ as excellent electrocatalysts for the hydrogen evolution reaction. *Nano Energy* **2021**, *90*, No. 106533.
- (92) Zhang, Y.; Liu, X.; Li, W.; Liu, W.; Yin, H.; Wang, D. Advanced and Durable Self-Standing MoC-Mo₂C Electrode for Alkaline Hydrogen Evolution in Chlor-alkali Electrolysis. *ACS Sustainable Chem. Eng.* **2023**, *11*, 9470–9477.
- (93) Zhou, Z.; Liu, Z.; Wang, Q.; Jia, Y.; Zhang, L.; Xiao, J.; Guo, L. Molten Salt One-Pot Electrosynthesis of a Ni-MoC-Mo₂C/Mo Self-Supported Electrode for Efficient pH-Universal Hydrogen Evolution. *ACS Appl. Energy Mater.* **2023**, *6*, 12084–12094.
- (94) Zhou, Z.; Wang, Q.; Yao, H.; Wang, M.; Wu, P.; Wang, H.; Zhang, L.; Guo, L. Rapid Synthesis of C₆₀-MoC Nanocomposites by Molten Salt Electrolysis for Hydrogen Evolution. *J. Electrochem. Soc.* **2023**, *170*, No. 026503.
- (95) Liu, W.; Wang, X.; Qu, J.; Liu, X.; Zhang, Z.; Guo, Y.; Yin, H.; Wang, D. Tuning Ni dopant concentration to enable co-deposited superhydrophilic self-standing Mo₂C electrode for high-efficient hydrogen evolution reaction. *Appl. Catal.*, B **2022**, 307, No. 121201.
- (96) Hughes, M. A.; Allen, J. A.; Donne, S. W. Optimized Electrolytic Carbon and Electrolyte Systems for Electrochemical Capacitors. *ChemElectroChem.* **2020**, *7*, 266–282.
- (97) Hughes, M. A.; Allen, J. A.; Donne, S. W. The Properties of Carbons Derived through the Electrolytic Reduction of Molten Carbonates under Varied Conditions: Part I. A Study Based on Step Potential Electrochemical Spectroscopy. *J. Electrochem. Soc.* **2018**, 165, A2608–A2624.
- (98) Hughes, M. A.; Allen, J. A.; Donne, S. W. The properties and performance of carbon produced through the electrochemical reduction of molten carbonate: A study based on step potential electrochemical spectroscopy. *Electrochim. Acta* **2018**, 278, 340–351.
- (99) Deng, B. W.; Chen, Z. G.; Gao, M. X.; Song, Y. Q.; Zheng, K. Y.; Tang, J. J.; Xiao, W.; Mao, X. H.; Wang, D. H. Molten salt CO_2 capture and electro-transformation (MSCC-ET) into capacitive carbon at medium temperature: effect of the electrolyte composition. Faraday Discuss. 2016, 190, 241–258.
- (100) Tang, J.; Deng, B.; Xu, F.; Xiao, W.; Wang, D. The lithium storage performance of electrolytic-carbon from CO₂. *J. Power Sources* **2017**, 341, 419–426.
- (101) Yu, R.; Deng, B.; Zheng, K.; Wang, X.; Du, K.; Wang, D. A facile strategy to synthesize graphitic carbon-encapsulated core-shell nanocomposites derived from CO₂ as functional materials. *Compos. Commun.* **2020**, 22, No. 100464.